SURFACE-INDUCED LAMELLAR ORIENTATION OF MULTILAYER MEMBRANE ARRAYS

THEORETICAL ANALYSIS AND A NEW METHOD WITH APPLICATION TO PURPLE MEMBRANE FRAGMENTS

NOEL A. CLARK, *Department of Physics, University of Colorado, Boulder, Colorado 80309*
KENNETH J. ROTHSCHILD, *Department of Physics and Department of Physiology, Boston University, Boston, Massachusetts 02215*
DAVID A. LUIPPOLD AND BRETT A. SIMON, *Division of Applied Sciences, Harvard University, Cambridge, Massachusetts 02138 U.S.A.*

ABSTRACT The orientation of membrane fragments into a lamellar array by a flat surface is analyzed. This analysis includes processes such as centrifugation and drying and physical effects due to membrane fragment steric interactions, finite size, elasticity, and thermal fluctuations. Several model calculations of optimal orientational order in multilayer membrane arrays are presented. The predictions of a smectic A model agree quantitatively with the measured spatial dependence of the fluctuations in layer orientation in a multilamellar array. A new technique, based in part on this analysis, for the preparation of well-oriented multilamellar arrays of natural and artificial membranes, isopotential spin-dry centrifugation, is described. The method involves the use of specially designed inserts for the buckets of a standard vacuum ultracentrifuge. The membrane fragments to be oriented are sedimented from solution or suspension onto a substrate of a convenient material which forms a gravitational isopotential surface at high g. Sedimentation is accompanied by removal of the suspending medium at high g to produce oriented films with a selected degree of solvation. In addition, a method is described whereby small solute molecules can be maintained in constant concentration with the membrane fragments during this process. Initial application of the method to the orientation of purple membrane fragments is described. The degree of orientation obtained in this system is evaluated using freeze-fracture and scanning electron microscopy, optical birefringence, linear dichroism, and microscopy.

I. INTRODUCTION

Oriented lamellar membrane arrays are extremely useful for probing membrane structure. For example, x-ray (1–12), neutron (10, 13–17), and light scattering (18–20, 34), optical (5, 15, 27–32), and infrared dichroism (33), and birefringence (18, 34) techniques all have been effectively used to study oriented natural and artificial membrane preparations. In the case of biological membranes, a variety of methods have been employed to produce oriented samples. These include drying suspensions onto surfaces (4, 5, 9, 13, 17, 21, 30–33, 35), shearing

---

Dr. Luippold's present address is the PPG Fiber Glass Technical Center, Pittsburgh, Pa. 15230.

between flat plates (36), centrifugation (1, 6–8, 11, 16), preferential orientation at interfaces (36, 37, 38) and electric (39), magnetic (15, 29), and black lipid film (28) techniques. In addition to these methods, multibilayer deposition (40) and annealing between flat plates (18, 34) have been successfully employed to prepare oriented artificial membrane (lipid bilayer) samples.

Despite numerous studies of oriented membrane samples, the approach to orientation has been largely empirical. For many techniques, basic questions with regard to the physical mechanisms of orientation, the intrinsic or practical limits to the degree of orientation, and how the process might be improved, remain unanswered. Since the production of thicker, better oriented biomembrane samples which retain biological activity would facilitate a number of biophysical investigations, we have been led to consider the basic physical processes affecting the orientation process. Much of our analysis is based on recent progress in understanding the elastic and mechanical properties of liquid crystals, which are formed by or closely related to multilamellar artificial and natural membrane arrays.

A large class of orientation methods are based on surface orientation: the penetration of the orienting influence of a flat or nearly flat surface into an adjacent volume densely packed with anisotropically shaped membrane fragments. In particular, centrifugation and drying, the two orienting methods widely used in biophysical studies of natural membrane systems, depend on surface orientation. We present models for surface orientation and discuss the relevant physical processes and parameters, showing that there is an intrinsic limit to the degree of lamellar orientation that can be obtained in a surface oriented sample. We discuss here only nonpolar lamellar ordering. We do not deal with questions concerning the nature of "face up or down" ordering in an array of asymmetric membrane fragments.

We then describe a new orientation method, isopotential spin-drying (ISD), which we have developed with the above theoretical considerations as a guide. In this method, isopotential centrifugation and drying at high g are used to partially order a membrane array and then to control the surface configuration of the suspending medium as it is removed and the array fully ordered. Finally, we detail the application of this method to orientation of fragments of the purple membrane of *Halobacterium halobium*. The resulting oriented films are used to evaluate the ISD technique in the light of our general considerations of the surface orientation process. Results on the application of the ISD technique to photoreceptor membrane and information obtained about rhodopsin is reported in two accompanying articles (41, 42).

II. THEORY

A. Surface Induced Orientation of Model Membrane Fragments

We use the term membrane fragment suspension to describe a variety of preparations which are suspensions of physically separate or loosely attached finite-sized membrane sheets. These sheets may be single- or multilayer, artificial or natural, and may be simply of multiply connected. Examples include cell plasma membrane fragments, purple membrane, whole cell envelopes such as erythrocyte ghosts or other closed natural membrane structures, rod outer segment disks, closed bilayer or multibilayer vesicles, and swollen multibilayer arrays. To gain some basic understanding of the orientation process, we begin with a single layer, circular flat

membrane sheet as the model of the entities to be oriented. We then consider problems encountered with more complex systems.

The primary factor operative in membrane fragment orientation by centrifugation or drying is the steric interaction of the anisotropically shaped membrane fragments with themselves and with a flat or nearly flat surface. In addition to steric forces we can expect that electrostatic interactions between membrane sheets will also be important, in fact dominating at larger sheet separation and controlling the relative face orientation of adjacent sheets, e.g., membranes having oppositely charged surfaces will tend to orient with all similar faces in the same direction. However, the lamellar ordering ultimately obtained under conditions of dehydration or low humidity will be determined by steric interactions and we will limit the present discussion to these. To illustrate this process we consider two models of the membrane orientation process. In the first, discussed in Appendix A and illustrated in Fig. 1 *a*, the membrane fragments are modeled by thin, hard disks (thickness = a, diameter = d, $a < 0.1$ d). In the second, more realistic model (Appendix B and Fig. 1 *b*), the membranes are permitted to be flexible and compressible, allowing us to treat the array as a bulk smectic A liquid crystal.

We characterize local orientation by a unit vector $\hat{n}(\mathbf{r})$ or by the polar angles θ, ϕ which give orientation of $\hat{n}$ at a point $\mathbf{r}$. It is also convenient to define $\delta\mathbf{n}$, the projection of $\hat{n}$ onto the orienting surface (xy plane, Fig. 1 *a*). For the hard disk model, $\hat{n}$ is normal to the disk centered at $\mathbf{r}$. As the disks pile up they will in general rest unevenly on their neighbors nearer the surface so that $\delta\mathbf{n}$ for a typical disk will be nonzero, as is shown schematically in Fig. 1 *a*. For the smectic A model $\hat{n}(\mathbf{r})$ is a continuous unit vector field locally normal to the layers. In this

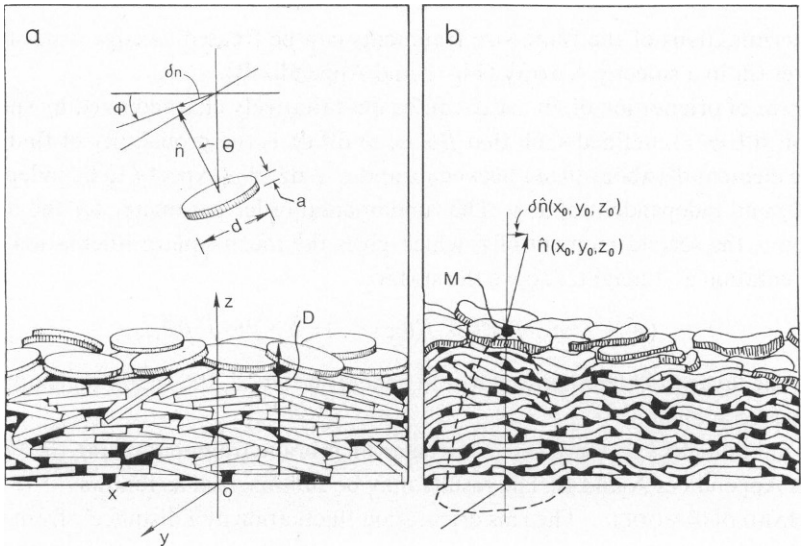

FIGURE 1 Illustrations of orientational disorder caused by finite fragment size in: (*a*) hard fragment disks; (*b*) flexible, compressible fragments. Only those fragment terminations which lie inside the indicated paraboloid of revolution will contribute to the layer tilt, $\delta\mathbf{n}$ (x_o, y_o, z_o) at point M.

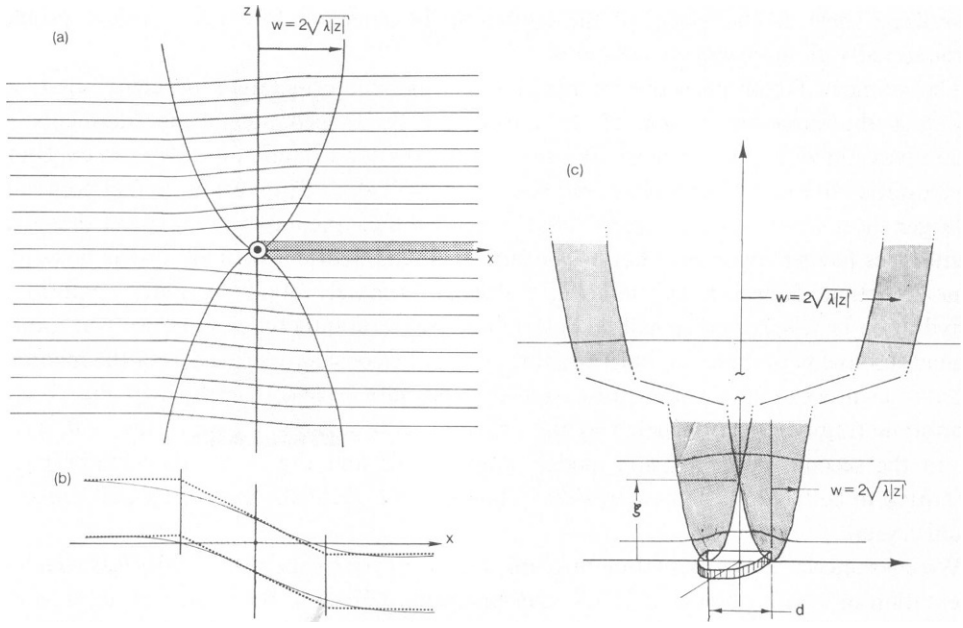

FIGURE 2 Layer displacement accompanying the termination of a single layer (heavy shading) in a smectic A liquid crystal (a unit edge dislocation) (45). (*a*) Significant layer tilt is confined to the lightly shaded parabolically spreading region $|x| < w = 2(\lambda|z|)^{1/2}$. (*b*) Dashed lines indicate the approximate layer distortion used in our calculations. (*c*) Distortion produced by a dislocation loop of diameter d and centered on the z axis in a smectic A. For $z < \xi$ the loop looks locally like a straight edge dislocation. For $z > \xi$ layer tilts produced by various parts of the loop overlap leading to maximum tilt near $r \simeq w$.

case, the terminations of the finite size fragments can be treated as edge dislocations which induce layer tilt in a smectic A array (Fig. 2 and Appendix B).

The degree of orientation of an array can be quantitatively characterized by specifying the distribution $f(\theta, \phi, z)$, defined such that $f(\theta, \phi, z)\, d\Omega\, dz$ is the probability of finding $\hat{n}$ in the solid angle element $d\Omega$ about (θ, ϕ) between z and $z + dz$. We expect f to be independent of ϕ ($\langle \delta \mathbf{n} \rangle = 0$) and independent of x, y. The fundamental order parameter for the orientational distribution is the second moment of f, which gives the mean square fluctuation in tilt from perfect orientation at a height z above the surface:

$$\langle \theta^2 \rangle_z = a \int\int d\Omega \cdot \theta^2 f(\theta,z) = 2\pi a \int d\theta \cdot \theta^3 f(\theta,z), \tag{1}$$

where a is the layer thickness; since θ will in general be small, the small angle approximation $\sin\theta \simeq \theta$ has been made.

The calculation of $\langle \theta^2 \rangle_z$ for arrays of circular membrane fragments using the two models is detailed in Appendices A and B. The results may be summarized as follows:

HARD DISK MODEL The rms orientation fluctuation at a distance z from the surface, $\langle \theta^2 \rangle_z$, is given by

$$\langle \theta^2 \rangle_z^{1/2} = (2z/3\xi_p)^{1/2} \quad z \leq \xi_p/3, \tag{2}$$

$$\langle \theta^2 \rangle^{1/2} \longrightarrow \langle \theta^2 \rangle_{\text{bulk}}^{1/2} \quad z \geq \xi_p/3, \tag{3}$$

where ξ_p is defined as the penetration length of surface induced order and is determined by the disk dimensions: $\xi_p = 2d^2/3a$. Far from the surface the orientational order is that of a bulk nematic of disk-like particles ($\langle\theta^2\rangle_{bulk}^{1/2} \lesssim 0.25$). Plugging numbers into the hard disk model results in $\xi_p = 260$ mm for pennies ($a = 1$ mm, $d = 20$ mm) and $\xi_p = 150$ μm for purple membrane fragments ($a = 5$ nm, $d = 1$ μm).

SMECTIC A MODEL Appendix B results from rms fluctuations are:

$$\langle\theta^2\rangle_z^{1/2} \simeq (z/z^*)^{1/4},\ z < \xi = d^2/16\lambda, \tag{4}$$

$$\langle\theta^2\rangle_z^{1/2} \longrightarrow \langle\theta^2\rangle_{bulk}^{1/2} \sim (\pi/32)\,(a/\lambda),\ z > \xi, \tag{5}$$

with $z^* \equiv d^2\lambda/a^2$. Here λ is the deGennes length (43, 44):

$$\lambda \equiv (K/B)^{1/2}, \tag{6}$$

where B is the layer compression elastic constant and K is the bulk layer curvature splay elastic constant, related to the commonly defined single layer curvature elastic constant k by $K = k/a$ (k is defined so that $\frac{1}{2}k(1/R_1 + 1/R_2)^2$ is the energy per unit membrane area at a place where the local orthogonal radii of curvature are R_1 and R_2) (44–46). Typically, $K \simeq 10^{-6}$ erg/cm, $k \simeq 5 \times 10^{-13}$ erg, $B \simeq 10^{+8}$ erg/cm^3, and λ is comparable to the layer thickness, a (43–46). Comparing this result to that of the hard disk nematic (Eqs. 2 and 3), we see that the smectic A model predicts a much slower variation of $\langle\theta^2\rangle_z$ vs. z with a characteristic penetration length, z^*, which is determined by both the fragment dimensions and elastic properties (through λ). The smectic A model predicts long range orientational order of the layers parallel to the surface with fluctuations characterized by $\langle\theta^2 B\rangle_{bulk}$, and an interfacial region of higher order adjacent to the surface, of thickness $\xi = d^2/16\lambda$, in which $\langle\theta^2\rangle_z^{1/2}$ varies as $z^{1/4}$. For many preparations the sample thickness will be smaller than ξ so that this interfacial behavior will determine the order (e.g., $\xi \simeq 5$ μm for purple membrane). This qualitative behavior persists for non-disk-shaped fragments, as long as the fragment surface dimensions remain large compared to a. In this case the ratio of fragment area to perimeter replaces d in Eqs. 4 and 5.

B. Disorienting Processes

Application of Eq. 4 to the membrane orientation process shows, in light of the relative constancy of the single membrane sheet thickness and elastic properties for various systems, that the mean fragment size d is the key variable parameter governing the quality of orientation of a surface oriented sample. Two membrane properties were implied in obtaining this result. It was assumed that fragments are flat, i.e., that they possess no intrinsic curvature, and that they will pack tightly together. Since breakdown of either of these conditions can significantly reduce z^* by increasing the effective a/d ratio of the fragments, they warrant further discussion.

There is considerable evidence that biological membranes are asymmetric (one face differs from the other), implying that they will in general possess intrinsic curvature. This effect has been observed in, for example, erythrocytes (R_s = radius of spontaneous curvature $\simeq 1$ μm) (49), whole bilayer vesicles ($R_s \geq 6$ μm) (50, 51), and nonhomogeneous multicomponent asymmetric bilayers ($R_s \simeq 40$ nm) (52). Secondly, membrane fragment layer terminations are

energetically unfavorable, promoting the formation of closed structures, such as vesicles. Typical membranes appear to have a weak but finite curvature elastic constant ($10^{-12} > k > 10^{-13}$ erg) (46), implying that forces must be applied to flatten out nonplanar membranes. Even very nearly planar membrane fragments can exhibit curvature: (*a*) in the presence of chemical inhomogeneities; (*b*) by landing on the stack folded over; and (*c*) as a result of thermal fluctuations (53), as discussed below.

Membrane curvature can decrease the degree of possible orientation by increasing the effective ratio of the membrane fragment thickness to width, $a/d \equiv \mathcal{R}$. This effect can be substantial. For example, the stacking of closed vesicles which remain spherical produces no orientation, and erythrocyte ghosts if completely flat have $a/d \simeq 10^{-3}$ compared to $a/d \simeq 0.2$ for the disk form in vivo. Therefore, to produce the best possible orientation, membrane fragments must be flattened out in addition to being deposited on the orienting surface. We can estimate in simple situations the forces necessary to render membrane fragments flat. We consider two geometries, the first being a spontaneously sinusoidal membrane (Fig. 3 *a*), having an undulation $u(x) = h \cdot \cos(qx)$ of wavelength $\lambda = 2\pi/q$ and amplitude h, which can serve as a model for any nearly flat fragment of average radius of spontaneous curvature R_s and average distortion amplitude h (e.g., Fig. 3 *b*). This model gives $(R_s^2)^{1/2} = (\langle(d^2u/dx^2)^2\rangle)^{-1/2} = 2/(hq^2)$. When flattened by application of pressure P to the bounding surfaces, the stored mechanical energy per unit area will be $U_m = \frac{1}{4}kq^4h^2$ with a corresponding pressure:

$$P = \tfrac{1}{2}kq^4h = k/hR_s^2. \tag{7}$$

For a distortion of mean radius $R_s \simeq 100$ nm and height $h \simeq 10$ nm we find $P \simeq 10^4$ dyn/cm^2. A second situation of interest is the flattening of a vesicle or of a membrane fold. Referring to Fig. 3 *c* and *d*, if we reduce the fold radius to a small radius r, we will store an energy $\pi k/2r$ per unit length of fold requiring a force per unit length $F = \pi k/2r^2$. Letting γ be the average layer area per unit fold length we obtain the required pressure:

$$P = F/\gamma = \pi k/(2r^2\gamma). \tag{8}$$

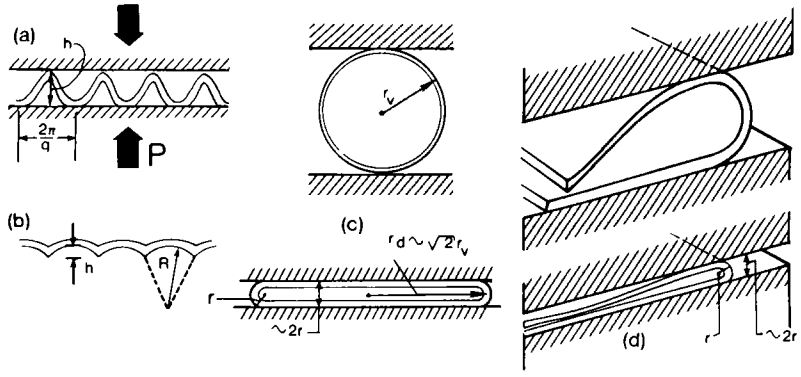

FIGURE 3 (*a*) The sinusoidally undulated membrane, a general model for a non-planar membrane; (*b*) example of a membrane with a radius of curvature R and height h; (*c*) geometry for the flattening of a spherical vesicle; (*d*) geometry for the flattening of a fold.

For vesicles of radius r_v which flatten to disks of radius $r_d \simeq 2^{1/2} r_v$, we find $\gamma \simeq (2r_d)^2/2\pi r_d$ and

$$P = \pi^2 k/(4r^2 r_d). \tag{9}$$

To completely flatten (i.e., make $r \simeq a$) a closed packed layer of 0.1 μm Diam disks ($r \simeq 10$ nm, $r_d \simeq 50$ nm) takes a pressure $P \simeq 2 \times 10^5$ dyn/cm^2. This pressure should, however, be considered to be an upper limit since the membrane may reach its linear elastic limit at a curvature radius larger than $r \simeq a$, in which case fracture at a weak point or plastic deformation may occur.

Even in the case of intrinsically planar membrane sheets, for compaction to occur, thermal layer bend fluctuations from planarity must be suppressed by the application of a compacting pressure P_{th}. Since thermal fluctuations are ubiquitous, P_{th} (δ) represents the minimum pressure required for compaction, such that the spacing between adjacent sheets is δ. P_{th} (δ) becomes nonzero as δ is reduced below the rms bend amplitude of a single sheet, δ_{th} (the rms thermal fluctuation amplitude of the lowest order bend mode of a single free membrane sheet of dimension d will be $\delta h_{th} = \langle h^2 \rangle^{1/2} \simeq d(k_B T/8k)^{1/2} \simeq 0.1\ d$). For $\delta < \delta h_{th}$, adjacent membrane sheets begin to "see" each other and steric repulsion will reduce δh. Helfrich (53) has shown that this reduction is accompanied by a decrease in entropy and therefore an increase in free energy. The result is an apparent elastic force resisting the compaction of a sterically repulsive layer array, characterized by a smectic A layer compression elastic constant $B \simeq k_B T/\delta^3$ (thus, at a level z in an array, a pressure $P_{th} \simeq k_B T/\langle \delta(z) \rangle^3$ is required to compact it locally). For $\delta \simeq 10$ nm, we have $B \simeq 4 \times 10^4$ dyn/cm^2. This result will be applied and discussed in the following section.

C. Orienting Processes

We now consider two widely used methods for obtaining oriented membrane fragment preparations: centrifugation and/or drying.

1. CENTRIFUGATION In centrifugal orientation, membrane fragments are sedimented from suspension onto the bottom surface of the suspension container. As the flux of membrane fragments intercepts this surface they are deposited layer by layer, ideally as in Fig. 1 *b*. Although centrifugation is an effective means of collecting the membranes onto the orienting surface, it does not generate pressures in the membrane array which are large enough to suppress significant spontaneous curvature or to flatten disks and folds. For example, a single membrane sheet which is 10% more dense than the suspending medium ($\Delta\rho \simeq 0.1$ g/cm^3) in an effective gravitational field $g_{eff} = 10^4\ g$ ($g = 980$ cm^2/s) will exert a downward pressure $P = \Delta\rho \cdot ga \simeq 1$ dyn/cm^2. ($g_{eff} = 10^4\ g$ was chosen for making estimates because it is readily accessible, not a limit intrinsic to our method discussed below, i.e., commercial centrifuges give $g_{eff} = 10^6\ g$.) Thus the bottom sheet of a 10-μm thick array will experience a pressure $P = \Delta\rho \cdot gD \simeq 10^3$ dyn/cm^2. An estimate of the largest compacting pressures achievable without great difficulty by centrifugation appears to be $P \simeq 2 \times 10^6$ dyn/cm^2. Comparing these estimates of P to those in section IIB, we see that centrifugation can effectively compact nonplanar membrane fragment arrays only when pushed to its limits and even then only at the bottom of the array.

Furthermore, even for flat membrane sheets, thermal fluctuations are not effectively suppressed by centrifugation. For an array equilibrated in a gravitational field of local layer

spacing $\delta(z)$, the layer compressional elastic constant at level z, according to the discussion in section IIB, must be $P(z) \simeq k_B T/\delta(z)^3$. For typical centrifugation pressures we have $\delta >$ layer thickness a and the overall thickness D_{sed} of a sedimental array and its layer spacing profile, $\delta(z)$, in a centrifugal gravitational field g_{eff} will be controlled by thermal layer bend fluctuations. D_{sed} and $\delta(z)$ may be obtained by using the equation for the decrease of pressure $P(z)$ with increasing z in the array $[dP/dz = -\Delta\rho \cdot a g_{eff} \cdot dn(z)/dz = -\Delta\rho \cdot a g_{eff}/\delta(z)]$. The minimum value is $P = \Delta\rho \cdot a g_{eff}$ at the top of the array ($z = D_{sed}$). Combining this with $dP = -B\,(d\delta/\delta) = -(k_B T/\delta^3)\,(d\delta/\delta)$, we find a thickness $D_{sed} = \delta_{max} N^{2/3}$ for a stack N layers thick. Here $\delta_{max} \simeq (kT/\Delta\rho\, a g_{eff})^{1/3}$ is the maximum thermal layer spacing which occurs at the top of the stack. Typically $\delta_{max} \simeq 1$ μm holds, so that D_{sed} is much larger than the fully compacted array thickness $D = Na$, i.e., centrifugal sedimentation can only loosely compact even membrane fragments which are flat in equilibrium. In a loosely compacted array the effective ratio of layer thickness to width is $\delta/d >> a/d$ leading, via Eqs. 4 and 11, to increased orientational disorder over the fully compacted array.

2. DRYING In comparison to centrifugal compaction, drying can exert, via capillary suction, much larger compacting pressures on a fragment array. Consider the drying of a membrane array. Initially the solvent evaporation causes the membrane fragments to be squeezed into a reduced volume, forming a loose array. Continued evaporation produces a solvent meniscus having regions of inward surface curvature with continually decreasing radii of curvature which draw the remaining solvent from between the membrane sheets, thus further compacting the array. For a 10^{-6}-cm gap between two membrane sheets in aqueous suspension the capillary pressure is $P = \sigma/r = 10^8$ dyn/cm^2, where $r = 5 \times 10^{-7}$ cm, and the surface tension $\sigma = 70$ dyn/cm. Depending on the rigidity of the sheets involved, this process could lead to either a tightly compacted array in which all of the space betweeen the sheets is eliminated or a porous spongelike structure with the sheets only partially in contact. For a membrane array, even with significant spontaneous curvature, the former case will apply. To see this we consider the collapse of a bilayer tube of radius R by drying (Fig. 4). To collapse the tube to a small thickness $t \simeq 2r$ requires a force (energy per unit tube length)$F_l \simeq$

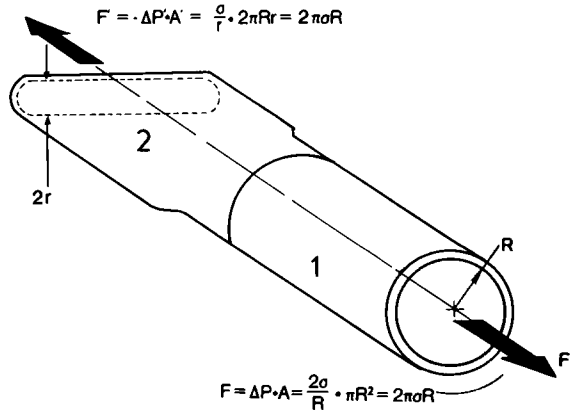

FIGURE 4 Geometry for the flattening of a bilayer tube by capillary suction. The initial state is illustrated in part 1 of the tube, the partially collapsed state in part 2.

$(k/2r^2)(2\pi r)$. If the minimum thickness is to be attained, i.e., $r \simeq a$, then $F_1 \simeq \pi k/a = \pi K$. The energy available due to capillary suction per unit collapsed tube length in this process (Fig. 4) will be $F = \Delta P(\pi R^2) = F' = \Delta P'(\pi Rr) = 2\pi\sigma R$, where σ is the surface tension. Capillary suction will collapse the tube for $F > F_1$, that is for $R > K/\sigma \simeq (10^{-6}/10)$ cm $\simeq 10^{-7}$ cm. Since the inequality is satisfied even for R as small as the sheet thickness a, essentially any gap between membrane sheets, including folds and disk edges can be collapsed by capillary suction. Drying should thus produce a compact array.

A second important aspect of the drying process is reorientation dynamics. As the concentration of fragments in the suspending medium is raised, steric repulsion of adjacent anisotropically shaped fragments leads to increased local parallel orientational correlation (43). As a result, it is not single fragments which interact with the surface but rather larger orientationally correlated groups of fragments. The reorientation dynamics of the fragments will be controlled by the size of the groups. Larger groups have a lower orientational mobility (43), and therefore respond more slowly to the influence of the surface. At sufficiently high concentrations there will be a transition to a (nematic) phase discussed above, which possesses macroscopic (but not necessarily uniform) orientational order. For anisotropic fragments of known shape, the critical concentration for this transition, c^*, can be estimated, and for purple membrane fragments is as low as $c^* \simeq 30$ mg/cm^3. (Recent attempts to magnetically orient purple membrane suspensions at concentrations above ~30 mg/cm^3 have failed, probably for this reason [15].) Hence, as the fragments are concentrated by drying, they are orientationally frozen into a nematic texture. Although the state of minimum elastic energy in such texture would have the fragments parallel to the surface, as discussed in Appendix A, distortions and defects of the orientation field cost very little energy so that once established they are metastable and not readily eliminated by the surface. These collective effects thus facilitate the formation of macroscopic defects in the orientational field which can become locked into the array structure. Macroscopic defects which preserve the layer thickness (focal conics, for example) are readily generated in smectic-A-like layer arrays (43). Such defects readily appear in preparations which are simply dried because the influence of the surface and the mutual membrane interactions develop at the same time. By contrast, centrifugation, which deposits sheets layer by layer from dilute solution, minimizes this effect, since there is no interaction between sheets in the absence of surface influence (as long as $D < \xi$). For this reason centrifugation followed by drying has proved to be a useful technique (7, 11). Centrifugation produces an array which is only partially compacted but with orientation limited only by the effective a/d ratio. Drying then fully compacts the array, increasing a/d and the degree of orientation.

Additional important considerations on drying include the following: (*a*) High solute concentrations which develop as an array is dried from a suspending medium containing small ions in solution constitutes a serious drawback since many membrane preparations require or can be profitably studied with added salts. We describe in the next section a device which alleviates this problem. (*b*) The drying process can also be complicated to some extent by the capillarity of the suspending medium. In drying an array onto the bottom of a cell, for example, the solution meniscus will be nonplanar (Fig. 5 *a*), leading to thickness nonuniformity in the dried film. This problem is minimized using ultracentrifugation as discussed in the next section.

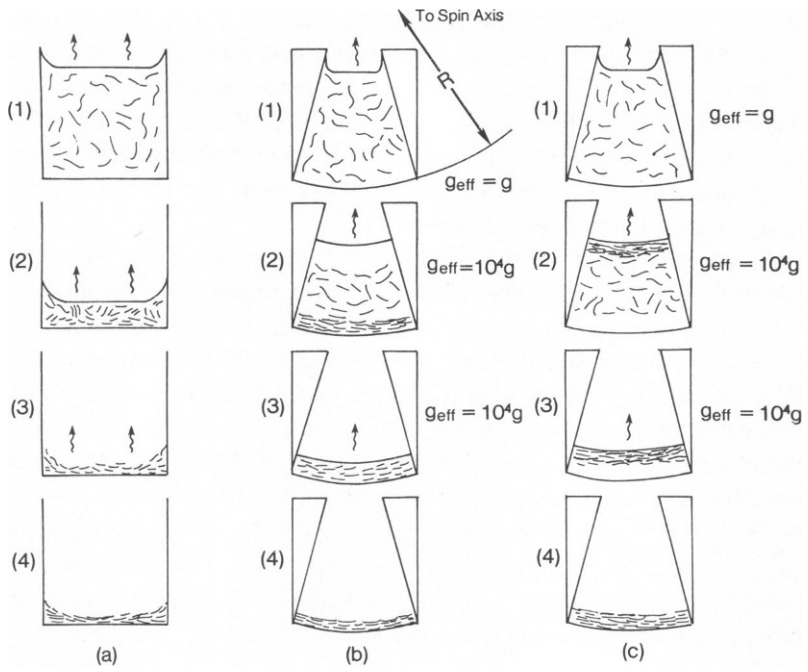

FIGURE 5 (*a*) Orientation by drying at $g_{eff} = 1$ g; mutual fragment interactions develop at the same time as fragment-surface interactions, a situation unlikely to produce optimal orientational order. Also capillarity leads to films of nonuniform thickness; (*b*) isopotential spin-drying (ISD): Fragments interact with each other only after the surface establishes orientational order. Surface deformation is suppressed by the large g_{eff}; (*c*) Spin-dry process for fragments less dense than the suspending medium.

3. EVAPORATION The rate of evaporation is an important factor affecting the formation of a well-oriented compacted array. Up to the time when the solution surface contacts the top of the deposited stack the evaporation rate is noncritical, although boiling or excessive sample cooling should be avoided. During the later stage of drying, when array compacting takes place, there are two possible modes of evaporation which we discuss with the aid of Fig. 6. Consider the evaporative closing of the solution filled space between two flat circular plates (membrane fragments of diameter d). At low evaporation rates capillary suction will pull the liquid air interface to the edge of the plates. The evaporating molecules will be replaced by fluid flow toward the edges of the plates, driven by capillary suction, and the plates will be drawn together as in Fig. 6 *a*. In this limit the evaporation rate controls the time dependence of the spacing, $u(t)$. Since capillarity induced flow will be limited by viscous stresses there will be some critical evaporation rate Q_c above which flow will be unable to compensate for evaporation. In this limit the fluid surface will recede into the space between the plates and the fluid will evaporate without drawing the plates together (Fig. 6 *b*). For the situation in which the surface tension forces dominate ($2\sigma/u$ larger than other pressures P_e) and the plates start with a spacing u_o, it can be shown that the critical evaporation rate (volume of fluid evaporated per unit area-time) is $Q_c = u_o\,\sigma/d\eta$, where η is the fluid viscosity. The smallest Q_c likely to be encountered in a membrane stack is quite large; for $u_o \simeq 10^{-7}$ cm, $d \simeq 10^{-4}$ cm, $\eta \simeq 10^{-2}$ g/cm-s, $\sigma \simeq 10$ erg/cm^2, we have $Q_c \simeq 1$ cm/s. In making this estimate

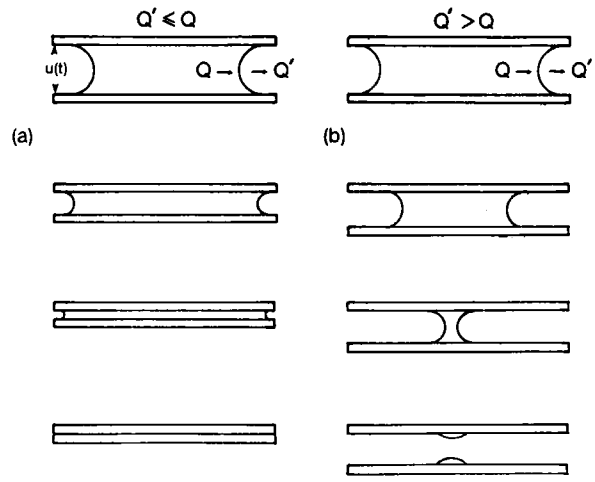

FIGURE 6 Model for calculation of array compression by evaporation. (*a*) Flat plates drawn together in an evaporation limited process; (*b*) if the evaporation rate is too large complete compaction will not be attained.

both membrane flexibility and the elastic forces tending to oppose compacting have been neglected. Inclusion of these will reduce Q_c somewhat. However, the drying rates employed in practice are conveniently made extremely low during compaction, in the range of 10^{-5} cm/s, and are therefore small enough to assure drying and compacting in the evaporation controlled limit.

To be flattened in a centrifugation-drying process, closed structures such as vesicles must be emptied of their contents. As a vesicle is squeezed down (Fig. 3 *c*) the resulting pressure difference ΔP which develops across the membrane will drive the drainage of the vesicle via either the normal solvent or solute membrane permeability at low ΔP (50) or by pores which may spontaneously grow to rupture the vesicle with significant probability at high ΔP (55, 56, 57). Drainage half-times for dipalmitoyllecithin (DPL) and egg lecithin (EL) vesicles were measured by Taupin et al. (57) and found to range from 300 min @ $\sim \Delta P = 10^6$ dyn/cm^2 to 5 min, $\sim 10^8$ dyn/cm^2 for DPL and were 200 times larger for EL vesicles (55, 56, 57). Hence, drainage under normal centrifugation pressures (10^5–10^6 dyn/cm^2) appears to be a slow process and may determine the minimum drying rate for some systems. Even under drying pressures (10^8 dyn/cm^2), EL drainage can be extremely slow.

III. METHODS, APPARATUS, AND PROCEDURE

A. General Methods

Many of the limitations of drying and centrifugation which we have cited can be avoided by a simple extension of presently employed techniques which permit layer by layer deposition as well as control of the surface configuration of the suspending medium. In particular, we have developed a procedure, isopotential spin drying (ISD), and apparatus in which drying occurs during centrifugation. A schematic drawing of the ISD apparatus is shown in Fig. 5 *b*. For this process to be effective, the surface upon which the fragments are to be deposited must form a gravitational isopotential in the corrdinate system

of the spinning cell. When the effective gravitational field is large ($g_{eff} >> g$) a cylinder coaxial with the spin axis will be very nearly a gravitational isopotential surface; such a surface will uniformly intercept the flux of sedimenting membrane fragments and the fragments once deposited will experience no gravitational force tangential to the surface. Hence, the deposited film will be uniform in thickness in contrast to deposition onto a flat surface wherein the fragments are forced into the corners. (For most situations the sedimentation takes place at low Reynolds number [$\eta/\rho \simeq 10^{-2}/cm^2/s$, $d \simeq 1$ μm, $v \simeq 10^{-2}$ cm/s, i.e., $R = \rho\, v d \eta^{-1} \simeq 10^{-4}$], implying laminar flow.) For anisotropic particles the sedimentation velocity will be $v_s = \Delta\rho\, vg\, \mu(\theta, \phi)$, where the anisotropic mobility μ depends on fragment orientation θ, ϕ. For disks, μ is largest for the disk plane parallel to **v**.

The suspending medium, taken for the moment to be salt free, is slowly evaporated while the centrifuge is spinning at high g_{eff}. This can be done, for example, by providing a sealed centrifuge cell containing the suspension with a small hole which allows slow solvent evaporation into an evacuated spin chamber. Drying while spinning is advantageous for the following reasons. First, while gravitational pressure alone cannot completely compact the stack it does so at least partially. Reducing g_{eff} before drying will therefore have the effect of allowing the stack to swell before being finally compacted which can only lead to disorder. Secondly, the solution surface is much more closely a gravitational isopotential surface at large g_{eff}. To see this we write U_s, the energy per unit area required to set up a sinusoidal surface undulation of amplitude u and wavevector q as $U_s = \frac{1}{2}(\rho g_{eff} + \sigma q^2)u^2$. For wavevectors, q, such that $q^{-1} > L = (\sigma/\rho g_{eff})^{1/2}$, the gravitational term dominates and renders the surface more difficult to distort than by surface tension alone. The length L is the distance over which the surface will be distorted by a local perturbation. At the cell wall, for example, the meniscus shape is given by $u(x) \simeq (\theta_o/q)\exp(-x/L)$, where θ_o is the contact angle. Thus, at large g_{eff} the capillarity induced surface distortion is much reduced ($L \simeq 0.3$ cm @ $g_{eff} = g$ and $L \simeq 0.003$ cm @ $g_{eff} = 10^4\, g$) promoting uniform fragment deposition and drying (Fig. 5 *b*, reference 3). Distortion of the solution surface as it comes into contact with the top of the partially compacted array is also suppressed at high g_{eff} so that thick spots that may occur tend to be reduced.

Up to this point we have dealt with membrane fragments which are more dense than the suspending medium. However, the techniques we have described can equally well be applied to fragments which are less dense than the suspending fluid. In this case, membrane fragments will sediment up to the solution surface which is also isopotential, thus forming a noncompacted, partially oriented array of uniform thickness (Fig. 5 *c*). Solvent evaporation will eventually produce the same situation as for the more dense fragments: stack compression between the bottom and solution surface isopotentials.

It is also possible to control the degree of hydration in the final compacted array. The solvent evaporation rate will be determined by the partial pressures of the evaporating components which are maintained over the solution surface. These may be varied over the course of sedimentation and compaction. The ultimate solvent content of the membrane array will be determined by the equality of the chemical potential of the remaining solvent with that of the vapor in equilibrium and thus by the partial pressures of the solvent components in the vapor. For example, the control of the degree of hydration of aqueous membrane arrays by manipulation of the chemical potential of water has been demonstrated (58). Similar techniques are readily applicable in connection with the methods described here.

B. Apparatus

Our centrifugation studies have been carried out using a Beckman Model L350 vacuum ultracentrifuge fitted with an SW 25.2 swinging bucket head (Beckman Instruments, Inc., Spinco Div., Palo Alto, Calif.). This head adapts three 100-ml buckets. The design of the centrifugation cell which we have developed to produce oriented membrane fragment arrays from salt-free suspensions is shown in Fig. 8. The primary element is the isopotential centrifugation cell (ICC), a single unit which forms the suspension cavity (SC) with the isopotential surface at the bottom. This unit is made to slide snugly but easily into the cylindrical part of the bucket. The hemispherical bucket bottom on which the ICC rests is filled with an epoxy plug, cast in place at high rpm to eliminate bubbles. Once cured the epoxy surface

was machined accurately flat and normal to the bucket cylinder axis. The apparatus is made to fit directly into the bucket, since standard bucket inserts do not fit the bucket to close enough tolerance and mechanically relax at high g_{eff}, leading to distortion of the ICC.

The ICC consists of a bottom plug and a cell body. The bottom plug was stainless steel with its top surface machined to within 0.010 in of being cylindrical and of the radius R_c equal to its distance from the spin axis when the buckets are fully swung out. For our ICCs made to fit the SW 25.2 head, R_c = 12.8 cm. To form the suspension cavity the bottom plug is fastened by two or more screws to the cell body which is made of delrin. The interchangeable substrate material upon which the membrane fragment array is to be deposited is clamped between the cell body and bottom as they are fastened together, thereby bending the substrate to conform to the cylindrical stainless steel surface. The substrate is sealed to the cell body by an "o"-ring, held in a groove on the cell body bottom. The cell body bottom is machined to the same radius R_c as the stainless surface, the slight change due to the finite substrate thickness being inconsequential up to 0.2 mm.

This design for the ICC permits the use of a wide variety of substrate materials, including those commonly required in the biophysical studies mentioned in section I. In general, as R_c is increased more materials are able to be bent without fracture. Substrates made from materials which could not be bent to R_c without breaking would have to be fabricated in a cylindrical shape. For the 12.8-cm radius isopotential of our apparatus, glass, and quartz microscope coverslips (0.2 mm thick) could be readily clamped to conform to the cell cylindrical bottom. We have successfully deposited oriented films on glass and quartz coverslips; plastic films from 6 to 200 μm in thickness made from Mylar, Glad Wrap (polyethylene), and Teflon; aluminum foil; AgCl, and KRS-5.

For drying, a small hole was introduced into the cap of the SW 25.2 bucket, through which the solvent passed into the centrifuge vacuum chamber. The holes were made by cementing Ealing pinholes (50 μm $\lesssim$ Diam $\lesssim$200 μm) over larger holes. Typical aqueous solvent volumes of 1–3 ml would evaporate in 4–10 h. This slow evaporation rate assured evaporation-limited compression of the partially compacted sedimented array, which forms relatively quickly after centrifugation commences. For example, purple membrane arrays were sedimented and partially compacted within 10 min with g_{eff} = 50,000 g.

The control of surface configuration while drying can be usefully exploited in other ways. Fig. 8 shows how an isopotential centrifugation cell discussed above is modified so that the salt or other solute concentration of the suspending fluid can be maintained constant during the sedimentation and compaction of a membrane fragment array. In this modified version (remote evaporation cell), evaporation takes place from a remote evaporation cavity (EC) which is connected to but distinct from the suspension cavity which holds the membrane fragment suspension. The EC and SC are connected by either a leak, a very narrow channel formed by the SC wall and the isopotential deposition surface (Fig. 8 *a*), or a porous or semipermeable membrane (Fig. 8 *b*). Evaporation from the SC is suppressed by capping it, although a small channel (CH) remains in the cap to allow pressure equalization as evaporation proceeds. In operation (Fig. 8 *c–e*) both cavities are filled, the SC with the suspension and the EC with the suspending with the level in the EC slightly higher. When the centrifuge is activated, hydrostatic pressure will induce flow of solvent from the EC to the SC until fluid surfaces in the EC and SC lie on a common gravitational isopotential. Centrifugation also sediments the membrane fragments to form a noncompacted array on the bottom (isopotential) surface of the SC. Controlled evaporation will occur at the solvent surface in the ED and as it does continued centrifugation will force solvent and solute from the SC to the EC, maintaining their surfaces on nearly a common isopotential which approaches the bottom isopotential. As long as this flow is maintained such that the hydrodynamic solute flux out of the SC is larger than the diffusion flux back into the SC, solute concentrations in the SC will remain constant and build up only in the EC. Comparison of the hydrodynamic and diffusional flux for an ideal solute shows that this condition requires a pressure difference between the ED and SC of $P_{ES} \gtrsim k_B T/\Delta^2 a$, where Δ is the channel dimension and a the solute molecule size, and is readily maintained. For deposition onto a semipermeable or porous surface on the one hand or with proper channel design on the other, essentially complete solvent removal without solute buildup in the membrane stack should be possible.

C. Procedure

We now discuss the preparation of oriented membrane preparations from suspending media without small solutes, using the basic ISD design of Fig. 7. Application of the remote evaporation cell for deposition from media with solutes (salts, etc., Fig. 8) will be discussed in a subsequent publication. In preparing membrane fragments for solute free orientation (Figs. 5 and 7), it is essential that the suspending medium be free of solvated small molecules. To remove small molecules, our membrane fragments were repeatedly resuspended and centrifuged in dust-free triply distilled water. Centrifugation proceeded until a well-defined pellet was formed. The supernate was then drawn off, the pellet resuspended and recentrifuged. This procedure was repeated typically at least three times until no trace of microcrystalline impurities were evident in the microscopic investigation of the dried sedimented arrays. In some cases dialysis of the fragment suspension against distilled water is performed. Freeze-fracture studies of the dried oriented arrays showed that macroscopic impurities such as dust particles can be a significant source of disorder. Therefore, in preparation of suspensions for sedimentation and drying, extreme care must be taken to prevent contamination by dust. A Nucleopore filter with 1-μm pore size was used to filter dust from the distilled water used for our suspensions. More importantly, since dust stuck to the cell walls is a major source of contamination, a high speed jet of this filtered water was employed to thoroughly wash all of the tubes for the preparative spins and the entire inside of the ICC before and after its assembly.

The purple membrane fragments used in this study were prepared using the method of Becher and Cassim (59). All spin-drying was done at 5°C with 1 ml suspensions of purple membrane having o.d. = 0.1–1.0 inserted in the ICC. Purple membrane purity was checked using SDS polyacrylamide electrophoresis and infrared and resonance Raman spectra which can detect minor sucrose and carotenoid impurity.

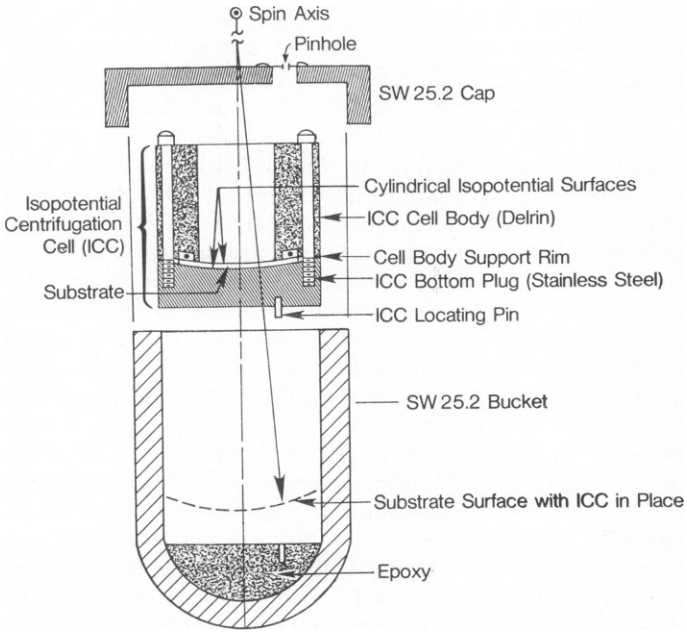

FIGURE 7 Schematic of the isopotential centrifugation cell (ICC) used in the experiments reported here showing the SW 25.2 bucket with the epoxy filler, the ICC which fits snugly into the bucket, and the SW 25.2 cap which seals the cell except for the leak through the pinhole to the centrifuge vacuum. Note that the delrin ICC body contacts the stainless steel bottom plug around its perimeter to minimize the compression of soft substrates.

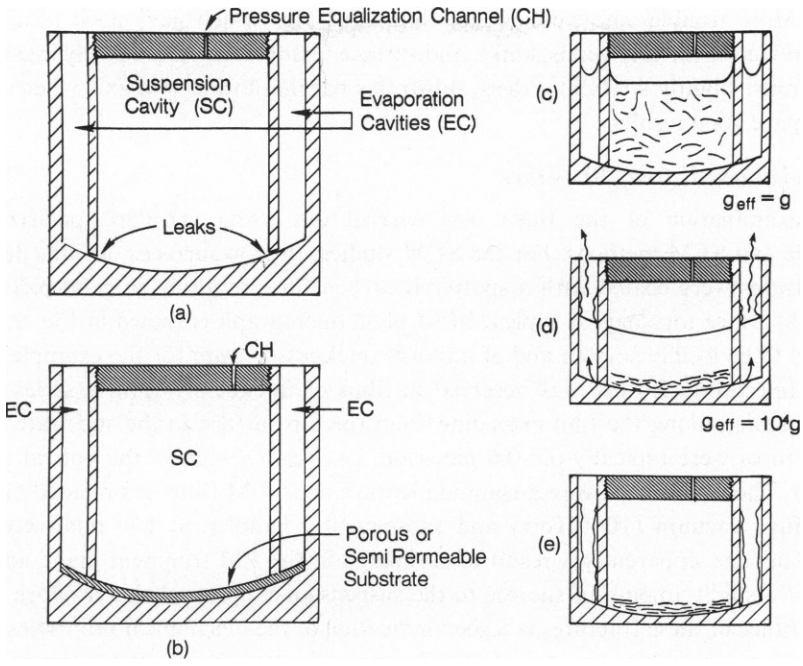

FIGURE 8 Remote evaporation isopotential centrifugation cells for sedimenting and compacting a membrane array while maintaining a constant salt concentration. Evaporation takes place in cavities (ECs) connected to the sedimentation cavity (SC) by leaks (*a*) or a porous membrane; (*b*) Evaporation from the SC is suppressed by a cap with a small channel (CH) for pressure equalization; (*c*)–(*e*) Schematic of the operating cycle for these ICCs.

IV. EVALUATION AND RESULTS

A. Introduction

We present here the results of optical, scanning electron microscopy (SEM), and freeze fracture studies aimed at evaluating the order in ISD oriented purple membrane (PM) arrays. These arrays were from 0.2 to 20 μm thick, prepared by sedimentation and drying from distilled water using the ICC of Fig. 8 as described above. Discussion of PM sedimentation and arrays from suspending media containing salts and sucrose using the remote evaporation cell of Fig. 7 will be continued in a subsequent paper.

PM was chosen for our initial studies because it can be stably suspended in distilled water at room temperature and because its well characterized structural and optical properties (60) provide for convenient evaluation of the arrays obtained. Since PM is strongly absorbing (ϵ = 63,000 ℓ/M–cm at 568 nm in isotropic suspension) visual and spectrophotometric inspection of its purple color provides a good assay of the uniformity of thickness of the array; thickness varied smoothly over the film area with no evidence of localized welts or bare spots, although incomplete washing of the suspension led to crystallite formation on the film and severe local thickness variation. Aluminum foil gave the best results, with <5% thickness variation across the whole 1.2-cm Diam film area. Glass and quartz coverslips also worked well, typically providing 0.4- to 1.0-cm Diam areas with a 5% variation and whole films with a 50%

variation. More troublesome were plastic film substrates which gave good results vis-a-vis glass only if free of the tiny bends, kinks, and surface textures which are easily introduced into such materials; slightly stretching these substrates parallel to the spin axis when assembling the ICC's gave good results.

B. General Array Structure

Detailed examination of the films was carried out using standard polarized opitcal microscopic and SEM methods. For the SEM studies, the top surfaces of films deposited on glass substrates were coated with a sputtered carbon film, resulting in good pictures of the films' local surface topology. A typical SEM photomicrograph is shown in Fig. 9. The films were found to be locally smooth and of uniform thickness (~4μm for the example of Fig. 9). The most interesting feature was observed in films of thickness >1μm: a series of vertical fractures running along the film extending from the top surface to the substrate (Fig. 9 *b*). These fractures were typically 0.2-0.6 μm wide, i.e., readily seen in the optical microscope (Fig. 10 *a*). These fractures were a common feature of all PM films sedimented and dried to the centrifuge vacuum (10^{-2} Torr) and subsequently handled at low relatively humidity (<25%). They are apparently a result of shrinkage in the PM fragment plane upon drying. Addition of a slight amount of sucrose to the suspension suppressed this fracture formation. The appearance of these fractures is a good indication of the mechanical properties of the PM films, as the membrane array acquires significant tensile strength parallel to the planes during drying. Dried PM films are quite rigid and brittle, much like thin crystals. When the thin plastic flexible substrates are used, bending it away from the PM film causes the film to break

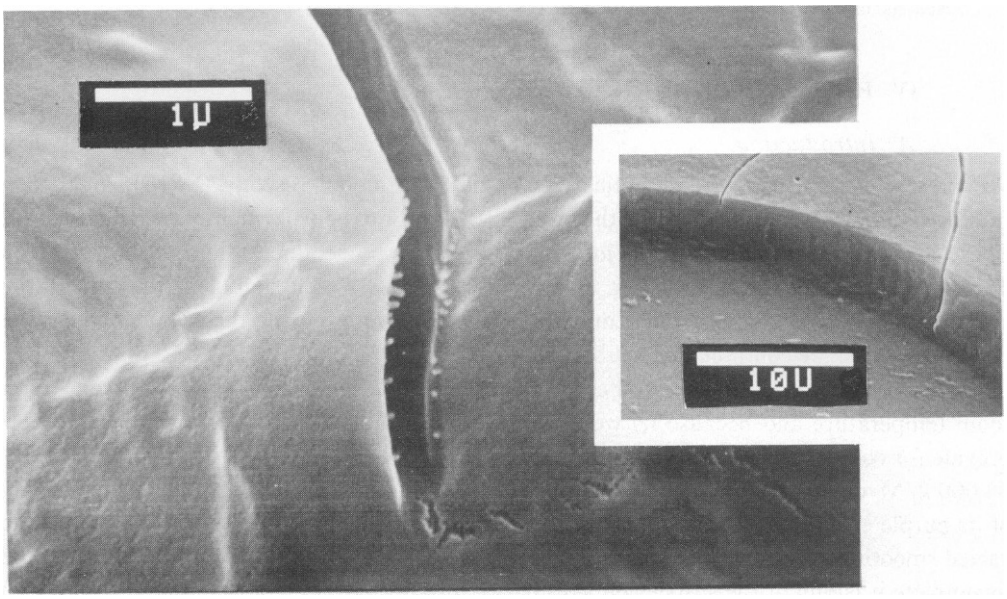

FIGURE 9 Scanning electron micrographs of the surface topology of films of multilamellar purple membrane arrays. Inset shows the smooth film for surface and the edge of the 4-μm thick film where a piece bounded by fracture lines has been removed from the substrate, visible in the lower half. A view of a typical fracture is also shown at higher magnification.

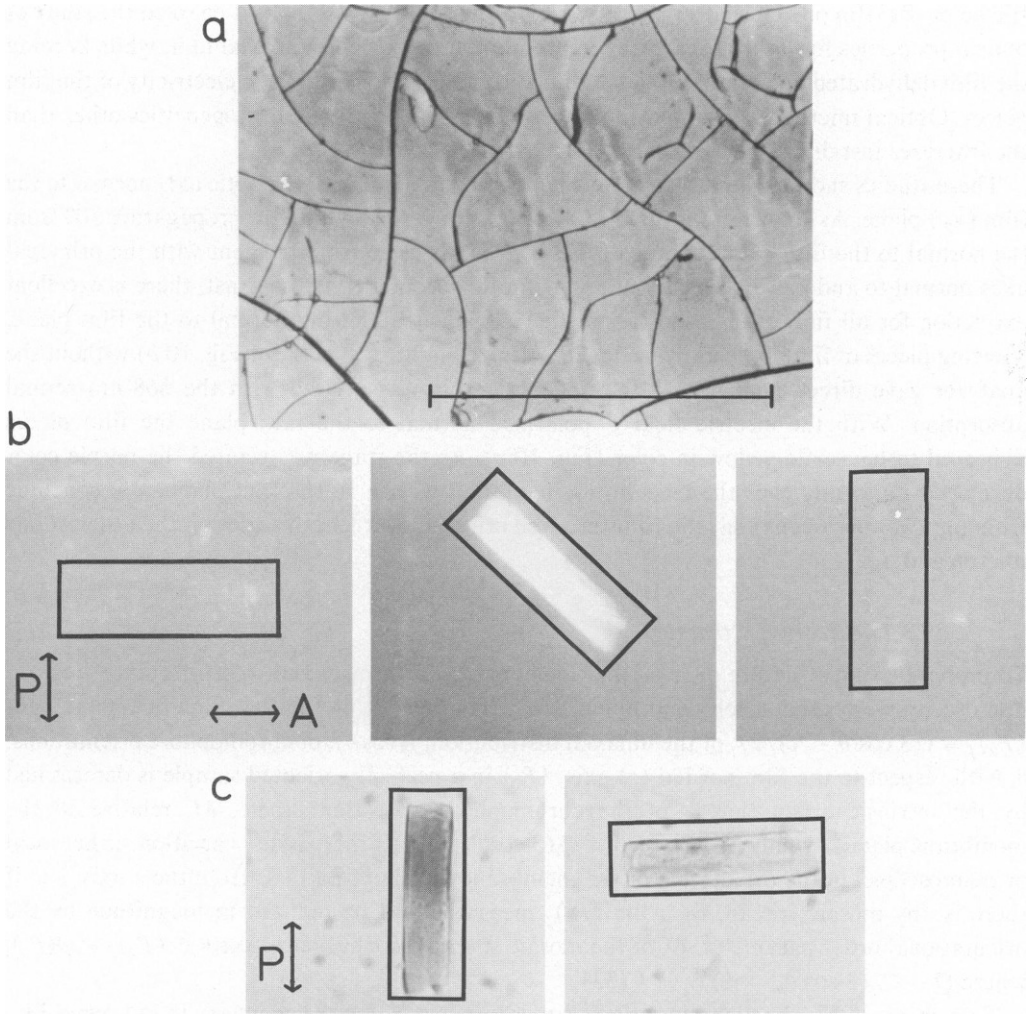

FIGURE 10 (*a*) Optical transmission photomicrograph of a membrane film showing typical fracturing; (*b*) Transmission photomicrographs between crossed polars (*P*, *A* = polarizer, analyzer orientation) of a film fragment suspended in paraffin oil and tipped up ~30° about its long axis out of the plane of the paper, demonstrating uniaxial birefringence (optic axis normal to film fragment plane); outlines added to indicate fragment position; (*c*) transmission of polarized 560-nm light by the film fragment of *b*, illustrating linear dichroism. Bar, 250 μm.

away in large (ca. several millimeters square) pieces, much like a thin sheet of ice from a flexed rubber surface. PM pieces ~0.5 mm across can be lifted from rigid substrates by sliding a razor blade across the substrate surface. Fractional film shrinkage upon drying was 3%, estimated from the average product of fracture width times length per unit film area. Partial rehydration of PM films by increasing the relative humidity of the surrounding air produced a closing of the fractures and a marked plasticity of the film.

Optical microscopy was carried out both on the deposited films and on pieces of the films removed from the substrates as discussed above and placed on glass slides or suspended in

silicon or paraffin oil. This latter preparation was particularly useful as it enabled the study of optical properties for light propagating in the film plane as well as normal to it, while keeping the film dehydrated and eliminating handling problems caused by static electricity of the film pieces. Optical microscopy showed the films to be free of optical inhomogeneities other than the fractures just discussed and occasional particulate impurities.

These studies showed the PM films to be optically uniaxial with the optic axis normal to the film (xy) plane. As shown in Fig. 10 *b*, a piece of film viewed with light propagating 30° from the normal to the film plane between crossed polars is clearly birefringent with the principal axes normal to and parallel to the film plane in this geometry. By contrast, there is excellent extinction for all film orientations about the z axis when viewing normal to the film plane. Viewing pieces of film tipped up on edge in polarized light (geometry of Fig. 10 *b*) without the analyzer gave direct evidence for the linear dichroism associated with the 568-nm retinal absorption. With the electric field E polarized normal to the film plane the film pieces appeared to be a pale yellow in color (Fig. 10 *c*). As the stage was rotated the purple color developed uniformly over the piece to its maximum with E in the film plane. We conclude from optical microscopy that the films are well oriented over length scales on the order of one micron and up.

C. Local Array Structure

To probe the film structure on a smaller scale, optical dichroism and freeze-fracture electron microscopy were used. Dichroism allows the measurement of the first significant moment $\langle P_2 \rangle_f = \langle (3\cos^2\theta - 1)/2 \rangle_f$ of the uniaxial distribution, $f(\cos\theta)$, of chromophore orientations, θ, with respect to the film normal (z) axis. $\langle P_2 \rangle$ in a perfectly oriented sample is determined by the intrinsic orientation θ_I of the chromophore transition dipole, M, relative to the membrane plane normal: $\langle P_2 \rangle_f = (P_2)_I = \frac{1}{2}(3\cos^2\theta_I - 1)$. If there is any variation, either local or macroscopic, in the orientation of the membrane fragment normals from the z axis, i.e., if there is any mosaic spread, then the $\langle P_2 \rangle_f$ measured will be reduced in magnitude by the orientational order parameter, Q, of the mosaic spread distribution $f_m(\cos\theta_m)$: $\langle P_2 \rangle_f = Q(P_2)_I$ where $Q = \langle \frac{1}{2}(3\cos^2\theta_m - 1) \rangle_{f_m} < 1$ (33).

To measure $\langle P_2 \rangle_f$ the dichroic ratio R is measured vs. α_o for the geometry in reference 33:

$$R \equiv \frac{\langle (\mathbf{E}_v \cdot \mathbf{M})^2 \rangle_f}{\langle (\mathbf{E}_H \cdot \mathbf{M})^2 \rangle_f} = 1 + \sin^2\alpha \frac{3\langle P_2 \rangle_f}{1 - \langle P_2 \rangle_f}, \tag{10}$$

where α is the angle between E_v in the film and the substrate plane and is given by Snell's law $\alpha = \sin^{-1}(\sin\alpha_o/n)$, where n is the film refractive index taken to be 1.50 and α_o is the angle of incidence. The weak optical anisotropy can be neglected here. R vs. $\sin^2\alpha$ should yield a linear plot with a unit intercept and a slope determined by $\langle P_2 \rangle_f$.

Visible dichroism measurements were made using a Cary 219 spectrophotometer (Cary Instruments, Fairfield, N.J.). PM films deposited on glass coverslips were mounted on a single axis goniometer by which they could be titled to any angle α_o around a horizontal axis arranged normal to the incident beam. A Glan-Thompson polarizer was placed before the sample in the beam. Spectra were measured at $\alpha_o = 0°$, 15°, 30°, 45°, and 60° for the polarizer set in the horizontal position, where the incident electric vector is parallel to the plane of the

film for all α_o, and in the vertical position, where the incident electric vector makes an angle α_o with the plane of the film.

Spectra were recorded from 700 to 400 nm at ±2-nm resolution. Each absorption spectrum was corrected by subtracting the absorption spectrum of the polarizer and the identical film bleached in methanol (so that the absorption maximum is shifted from 570 to 380 nm) appropriately oriented. This procedure eliminated artifacts due to the wavelength dependent transmission of the polarizer and glass on the polarized incident radiation and yielded spectra with flat baselines. The wavelength dependence of the Fresnel loss was neglected. Sample thickness D was obtained from A_P (58), the peak absorbance at 568 nm, using $D = A_p/[\epsilon c(1 - \langle P_2\rangle_f)]$, where $\epsilon = 63{,}000$ ℓ/M-cm and the concentration in the dried films $c = 0.035$ M/ℓ was determined by our freeze-fracture studies, described below.

Measurements of R vs. $\sin^2\alpha$ yielded a straight line as expected (Fig. 11) and were used via Eq. 10 to calculate $\langle P_2\rangle_f$. In an effort to assess the dependence of orientational order as film thickness $\langle P_2\rangle_f$ was determined for films of varying thickness over the range 1 μm $< D <$ 20 μm. Over this range in D the average value of $\langle P_2\rangle_f$ was found to be $\langle P_2\rangle_f = -0.28 \pm 0.06$ in quantitative agreement with previous measurements (31, 36, 37, 38). Assuming no mosaic spread ($Q = 1$) this $\langle P_2\rangle_f$ yields a transition dipole tilt angle of 67° ± 2° relative to the sample normal. There was, however, no discernable systematic dependence of $\langle P_2\rangle_f$ on thickness so that we could only set an upper limit of 0.05 on the increase of Q, as D increases from 1 to 20 μm. This result will be used in the next section.

D. Freeze-fracture Electron Microscopy

Freeze-fracture was used to visualize the local structure of our dried PM films. To obtain freeze-fracture replicas, a 0.5-mm square 10 μm thick film was removed from its glass substrate and broken into many small pieces which were suspended in paraffin oil. Since the film is rigid and brittle the pieces maintained their structural integrity, dichroism, and birefingence when suspended in the oil, as noted above. The pieces were collected together and the excess oil removed until a rather densely packed slurry was formed. A small drop of this slurry was placed on a copper disk and frozen in Freon-22 at 77°K. The frozen drop was

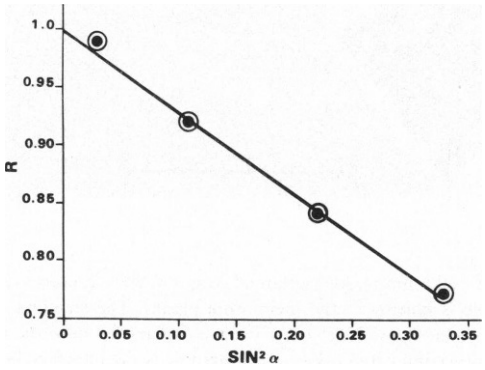

FIGURE 11 Linear dichroism of purple membrane film at 560 nm. Dichroic ratio, R, vs. $\sin^2\alpha$, α = sample orientation for a 10-μm thick purple membrane film.

fractured using a Balzers system (Balzers Corp., Nashua, N.H.) at 163°K and 2×10^{-6} Torr, and shadowed and coated with evaporated Pt-C. The resulting replicas were brought up to room temperature and pressure, suspended at the interface of toluene floating on water, and transferred via a thin wire loop to a bleach wash. Since the film pieces were isotropically oriented in the slurry, we obtained fracture faces both parallel and normal to the membrane planes.

Fig. 12 shows a region, roughly 0.6 μm square, of a fracture face typical of those for which the fracture surface is normal to the membrane planes. This normal fracture surface is characterized by a texture which is rough in comparison to that of the paraffin oil visible in the lower left corner of Fig. 12 *a*. The smooth paraffin oil face and the rough normal membrane array face are separated by a sharp straight boundary line (solid arrows). The array face exhibits a quasiperiodic set of lines which run nearly parallel to the boundary.

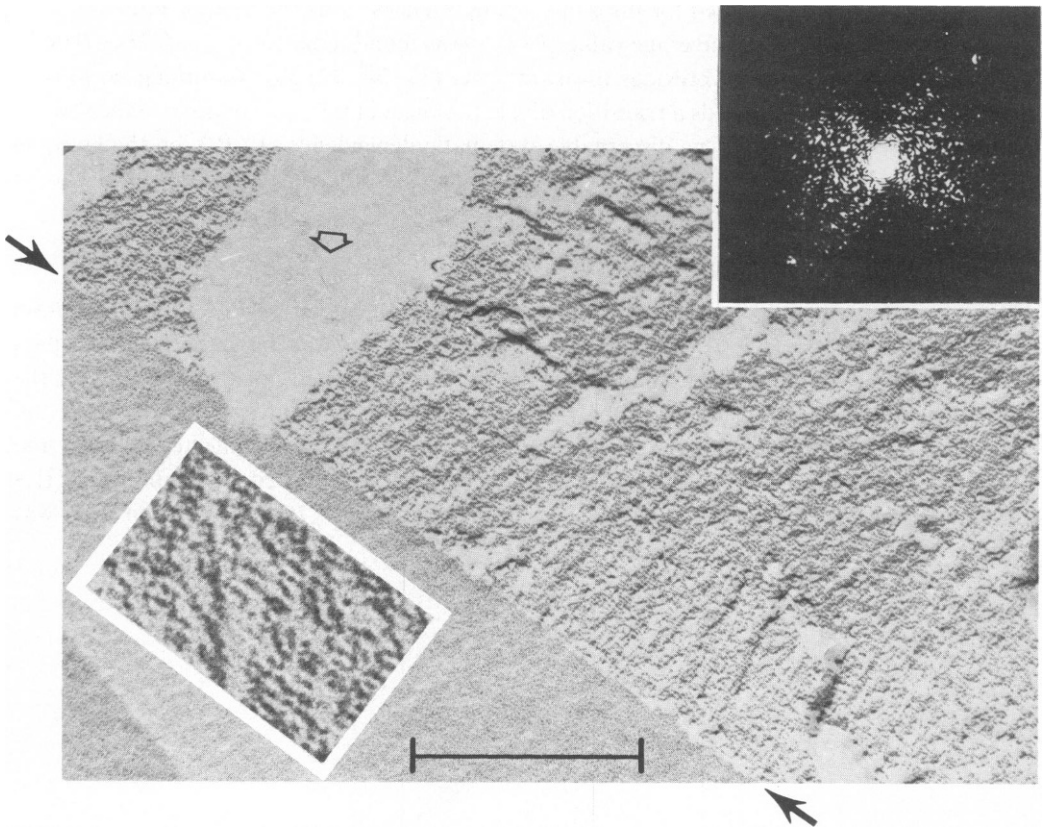

FIGURE 12 Typical face (~0.6-μm region) obtained from a freeze-fractured purple membrane array for which the fracture surface is normal to the membrane planes. The shadows are light with the shadow direction indicated by the open arrow. The sharp linear boundary between the rough (film fragment) and smooth (paraffin oil) textures, indicated by the black arrows, is the interface between the paraffin oil and the film fragment surface which contacted the glass during deposition. Bar, 200 nm. (insets) Close-up of a 75 × 120-nm region spanning 15 purple membrane layers, each 5 nm thick; laser optical diffraction pattern obtained from the transmission electron micrograph transparency of a 0.2 × 0.2-μm region of this fracture face. The spot splitting yields a lamellar repeat, $a = 4.98 \pm 0.05$ nm.

These lines, which are clearly evident at higher magnification (see lower inset of Fig. 12 *b*), typically appear as strings of dots running more or less parallel to the boundary. The optical diffraction pattern of a typical 0.2-μm square area of this face is also shown in the upper inset of Fig. 12 *c*. It consists of a single pair of diffraction limited Bragg spots and a diffuse background which is substantial over a region comparable in size to the spot splitting, with the exception of a dark band corresponding to the shadowing direction. The spot splitting yielded a value of $a = 4.98 \pm 0.05$ nm for the spacing of the lines on the fracture face. In view of the previously measured x-ray diffraction value of $a = 4.7$ nm (8) for the lamellar repeat distance in dried PM arrays we identify the lines in the normal fracture faces to be the terminations at the surface of the individual membrane sheets. Ten different faces on our replicas which showed the characteristic texture of Fig. 12 were studied by optical diffraction. Observed values of a were limited to the range $4.7 \text{ nm} < a < 5.1$ nm, indicating that these faces are nearly normal to the membrane planes. No faces which could be clearly identified as oblique were found, suggesting normal fracture to be a preferred mode in PM arrays.

Faces such as that of Fig. 12 were used to study orientational order in the dried film. Local layer direction was determined by projecting a transparency of the face onto a screen and tracing out the clearly visible layer endings to produce a facsimile such as in Fig. 13 in which the lines represent local layer-orientation. This entire surface facsimile was then partitioned with a convenient grid (20 × 40 nm for Fig. 13), the average orientation in each block noted visually using a drafting machine and recorded, and the orientation statistics calculated. Results for the face of Figs. 12 and 13 are shown in Fig. 14 *a*, which gives the distribution of orientations for the whole surface (920 blocks), θ, about the mean. The mean orientation is indicated as the dot-dash line in Fig. 13 and is determined to within $\pm 0.25°$ using the 920 blocks of the grid. As is evident the mean layer orientation is parallel to the boundary line, indicated by the heavy solid line, to within the accuracy that the boundary line direction can

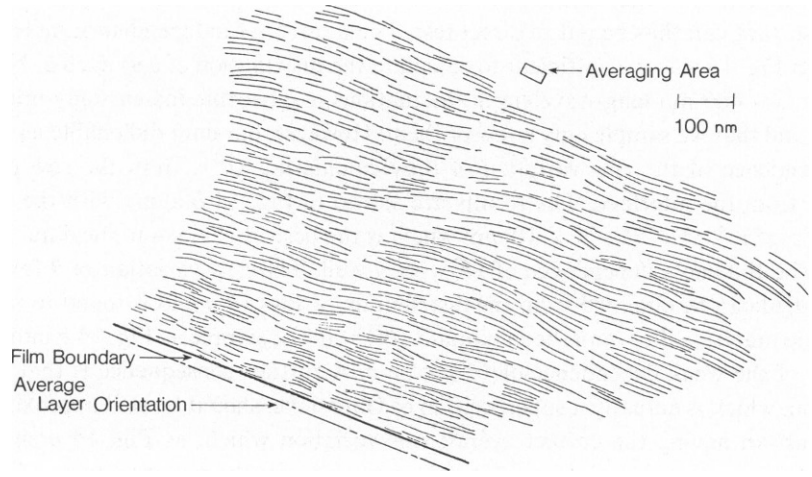

FIGURE 13 Facsimile of the freeze-fracture of Fig. 12 *a* made up of lines indicating the local layer-orientation. Dot-dash line shows the calculated average orientation to be parallel to the glass-film interface mentioned in Fig. 12 *a*. Distribution of orientations in 920 blocks (20 × 40 nm each) gave Fig. 14.

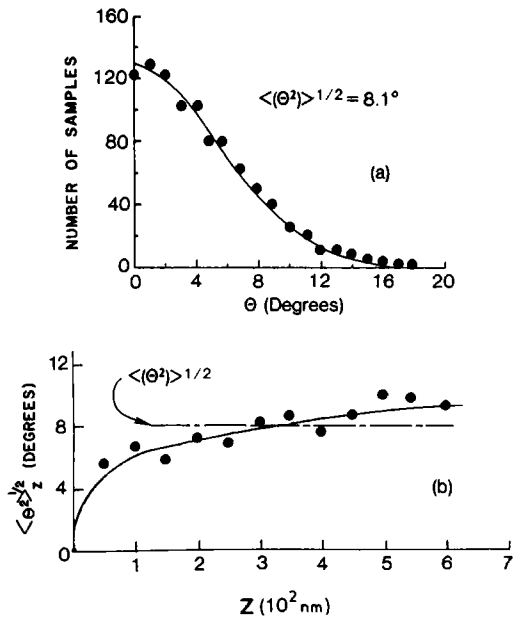

FIGURE 14 (*a*) Orientational statistics from average orientation in each grid block in Fig. 13, giving distributions of orientation in θ about the mean for the whole surface of 920 blocks; (*b*) dependence of rms variation of θ vs. thickness z above film-glass interface. The solid line is the best fit to Eq. 4 of the text.

be determined ($\pm 0.5°$). This, coupled with the observation that the layers nearer the boundary are very well ordered, leads us to conclude that the boundary is in fact the bottom surface of the film, i.e., the glass-film interface.

Our predictions for the dependence of the orientation statistics on distance from the orienting surface can thus be put to direct test. The number of independent samples of $\theta(x, z)$ available in Fig. 13 was not sufficient to calculate the distribution of θ at each z. Note in Fig. 13 that for $z > 400$ nm long-wavelength fluctuations in θ become increasingly important (as expected) and that we sample only a few of them. However, our data did enable us to measure the z dependence of the rms variation of θ by calculating $\langle\theta^2\rangle_z$ from the row of blocks a distance z from the interface. The results are shown in Fig. 14 *b* along with the solid curve $\langle\theta^2\rangle^{1/2} = (z/z^*)^{1/4}$, $z^* = 75 \pm 1 \times 10^5$ nm which is the best fit of Eq. 4 to the data. The theory describes the thickness dependence of $\langle\theta^2\rangle_z$ very well. The rms variation of θ for the entire region studied can be obtained from the distribution of Fig. 14 *a* and is found to be $\langle\theta^2\rangle^{1/2} = 8.1°$, not too much smaller than the maximum $\langle\theta^2\rangle_z^{1/2}$ in the sample as Fig. 14 *b* indicates. This is a result of the weak dependence of $\langle\theta^2\rangle_z^{1/2}$ on z. A further consequence is that the overall distribution, which is actually a superposition of Gaussians, should be well approximated by a single Gaussian having the correct overall rms variation which, as Fig. 14 *a* shows is also observed. Hence, our smectic A model is able to account for the major features of the surface region of this sample of the PM orientational distribution.

Extrapolating the solid curve of Fig. 14 *b* to 1 μm $< D <$ 20 μm, the thickness range over which the visible dichroism was studied (section IVC) yields a variation in the mosaic spread

order parameter from $Q = 0.94$ ($\langle\theta_n^2\rangle^{1/2} \simeq 11°$) at $D = 1$ μm to $Q = 0.77$ ($\langle\theta_n^2\rangle^{1/2} \simeq 40°$) at $D = 20$ μm, a decrease of $\Delta Q = 0.17$. This change of Q was not found in the dichroism data, as noted in the previous section, where $\Delta Q < 0.05$ was found. This observed lack of variation of Q for 1 μm $< D <$ 20 μm indicates that the bulk smectic order as discussed in Appendix B is established in this range. Since the freeze-fracture data of Fig. 14 suggest that the region of sample influenced by the surface is on the order of 0.5 to 1 μm thick, a reasonable estimate for the range, ξ, of surface induced order (see Eq. B7), is $\xi \sim (2 \pm 1)$ μm. With this estimate and taking $a = 5$ nm for purple membrane, it is possible to compute, using Eqs. B7–9, the effective fragment diameter, d, and deGennes parameter λ. The results are $d = (0.85 \pm 0.15)$ μm and $\lambda = (28 \pm 8)$ nm. These numbers are both quite reasonable ($\lambda = 10$ nm is obtained for dried dipalmitoyl lecithin multilayers [18]). The corresponding bulk mosaic spread, from Eq. B9 is $\langle\theta_n^2\rangle^{1/2} = 12° \pm 2°$, that is $Q = 0.92 \pm 0.02$. Including this Q into the analysis of the dichroism data yields an orientation order parameter for the transition moment of $\langle P_2\rangle_f = 0.30 \pm 0.08$, and a corresponding tilt angle of 69° ± 2°. We conclude from this agreement that the surface induced orientation of this portion of our PM preparation is optimized.

A question which might be raised with regard to these results concerns the effects of the fracture process on the orientational distribution of the layer terminations, especially since the fracture surface texture is so rough. While we have no quantitative information on this point we note that the dried PM film is quite rigid and brittle at room temperature, properties which we expect to be enhanced at low temperatures and to indicate resistance to plastic flow. Furthermore, although the rough fracture surface texture is accompanied by localized orientation variations (within the blocks of our grid), it is the longer wavelength layer undulations which gave the major contributions to $\langle\theta^2\rangle^{1/2}$ and these should be effectively frozen in the dried film at 77°K.

We now turn to the most prominent fracture mode observed in our replicas: fracture faces parallel to the layers. Typical parallel faces are shown in Fig. 15. These faces exhibited a terraced structure made up of nearly planar fractures over various sized areas of single membrane sheets. Areas up to 0.5 μm across were observed. As Fig. 15 shows, the parallel fracture faces are characterized by two distinct kinds of surfaces: either a rough texture surface formed by a quasi-periodic array of variously shaped aggregates of particles (P-face) or a much smoother surface which also exhibits a periodic structure (E-face). The identification of these surfaces follows from their similarity in appearance to faces found by Fisher and Stoeckenius (61) in the freeze-fracture of the plasma membrane of *H. halobium* and by Fisher et al. (62) in the freeze-fracture of PM fragments adsorbed to polylysine treated glass.

A typical sample of the P-face fracture surface and its optical diffraction pattern are shown in Fig. 15 *c*. The arrangement of particles on these faces is periodic on a two dimensional hexagonal lattice, having unit cells of edge dimension 6.0 ± 0.1 nm, comparable to that observed for PM adsorbed on glass (62). Although the P-faces produce first order Bragg spots which are diffraction limited, indicating the registration of particles onto a hexagonal lattice over distances on the order of 100 nm, it is clear from the photographs that there is significant local displacement of particles from their ideal 2-D hexagonal positions. To characterize this displacement of particles which presumably occurred during the fracture process, we superimposed on the negative an array of fine dark lattice lines (unit cell boundaries) having a spacing and orientation corresponding to the local diffraction limited Bragg spots. To achieve

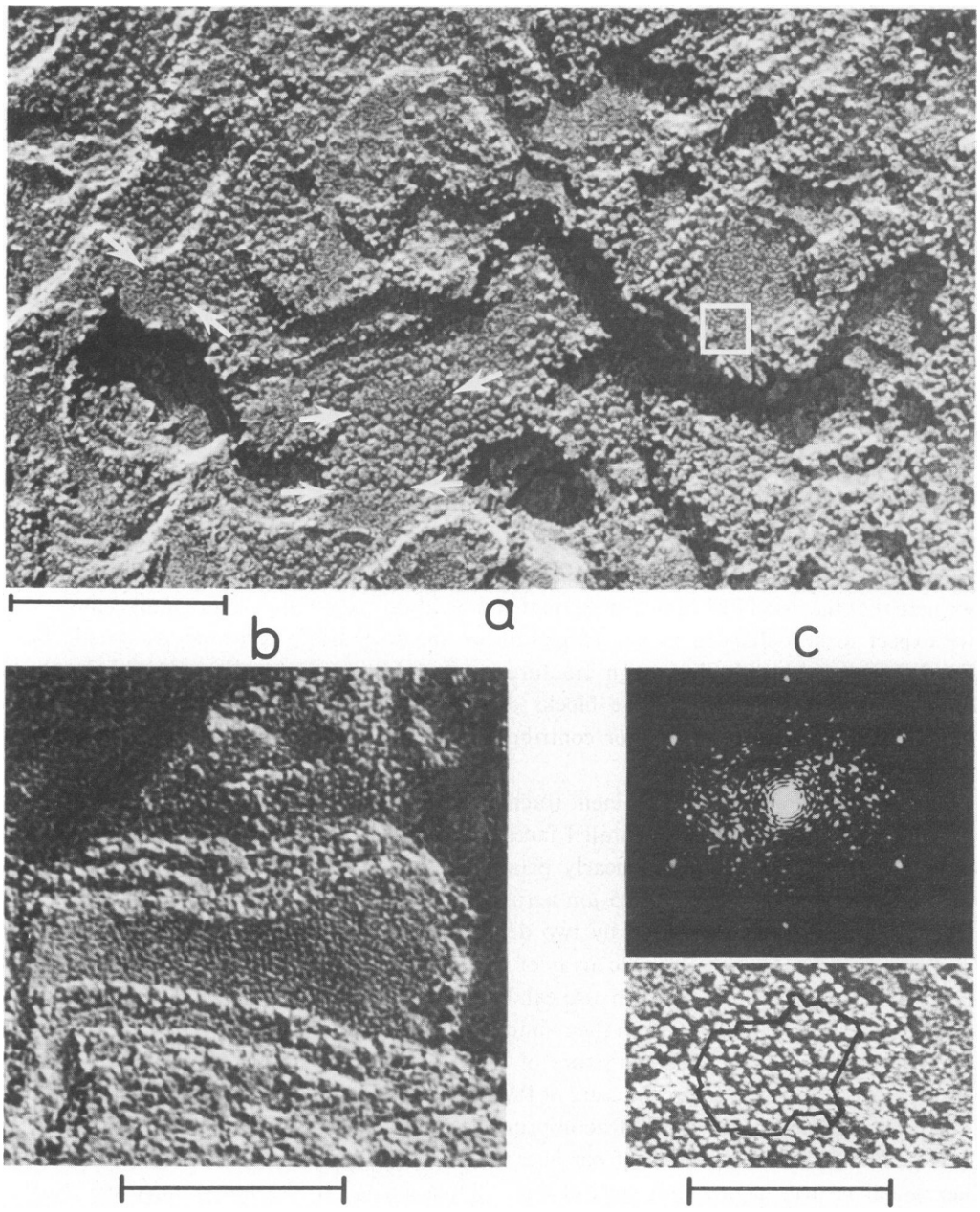

FIGURE 15 Parallel fracture faces (shadows dark): (*a*) typical terraced structure showing smooth endoplasmic E faces and rough protoplasmic P faces. White arrows indicate smooth E to P face transitions which indicate fracture surfaces located asymmetrically in the layers (see Fig. 17). White square shows a single aggregate of particles, pulled from the E face during the fracture, on an otherwise smooth P face surface. The P face area immediately to the right of the square shows a well ordered row structure. Bar, 200 nm. (*b*) Large P face area showing the hexagonally periodic $2d$ lattice structure. Bar, 155 nm; (*c*) Typical E face area and its optical diffraction pattern (spot spacing = 5.2 ± 0.1 nm, hexagonal unit cell side = 6.0 ± 0.1 nm). Individual protein trimers, visible as bright dots, are aggregated into particles of various size and shape. Fig. 16 shows the pattern of displacement and aggregation of the trimers from their ideal $2d$ hcp positions. Bar, 120 nm.

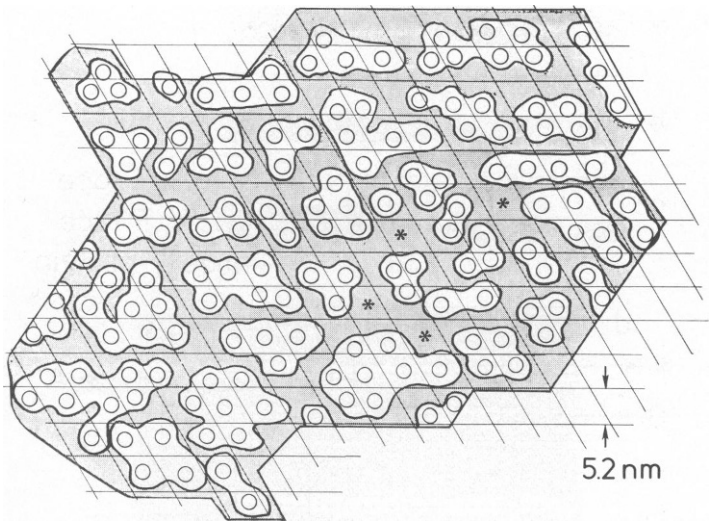

FIGURE 16 Schematic of region outlined in Fig. 15 *c* indicating the arrangement of light areas (electron dense regions) relative to the grid of 2*d*-hexagonal lattice lines determined from optical diffraction of the same area (Fig. 15 *b*). The lattice is positioned to optimize centering of the light areas on the parallelogram unit cells. The circles represent the approximate location of particles which have aggregated to make up the light areas. Unit cells whose contents cannot be accounted for are indicated by an asterisk. The common aggregates are the trimers and diamond shaped particles proposed by Fisher and Stoeckenius (61).

the optimum centering of particles on unit cells permitted by the structure, the brightness of the composite picture was maximized by translational positioning of the lattice line array such that an ideal 2-D hexagonal arrangement would have a particle centered on each unit cell. The location of the particles relative to the unit cell array was then recorded. The result, for a region of Fig. 15 *c* containing 170 unit cells is shown in Fig. 16.

The composite particles appear to be aggregates of roughly circular electron opaque regions, 4 nm in diameter. Each of these regions, presumably a protein trimer contributes to an aggregate. Materials from only a small percentage of the unit cells (denoted by asterisks in Fig. 16) could not be accounted for in this way. However, these missing cells may account for the appearance of occasional particles on otherwise smooth E-faces (white arrow, Fig. 15 *a*). Aggregates of from 1 to 10 unit cell contents were found, with the three-cell (triangular) and four-cell (diamond shaped [61]) arrangements being the most common.

The E-faces also exhibited 2-D hexagonal periodicity with lattice constants similar to those of the P-faces, but with a much smoother surface variation.

The typical area over which a planar fracture occurs in a particular membrane sheet is smaller in the purple membrane lamellar arrays than in whole cell (61) or single sheet fractures (62), probably a result of the multiplicity of potential parallel fracture planes in the lamellar arrays. Hence, whole cells or single sheets may be better suited to the study of the face structures than lamellar arrays. However, the switching of the fracture surface from one membrane sheet in the array to another as it proceeds through a lamellar array provides many examples of the termination of fractional, single, or multiple membrane sheets which can be used to gain information concerning the location of the fracture plane in a given membrane

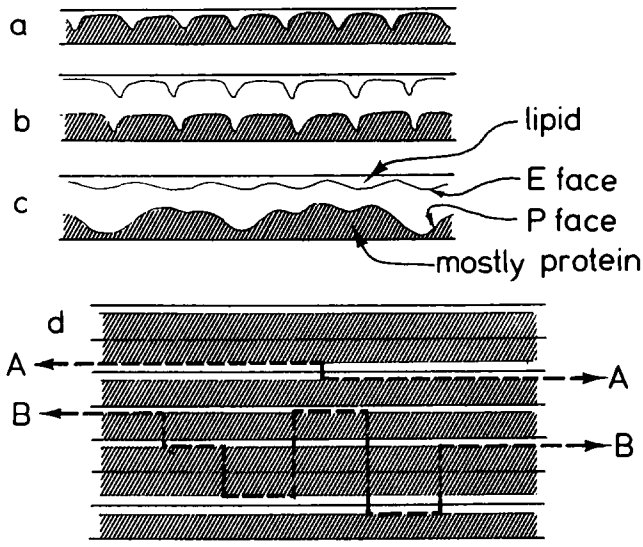

FIGURE 17 Model for purple membrane freeze-fracture: (*a*) schematic membrane before fracture; (*b*) membrane immediately after fracture. Only a small amount of material ends up on one side. Given the protein structure this may be primarily lipid. (*c*) After fracture, surface energy reduction drives plastic deformation and aggregation; (*d*) schematic of a randomly stacked purple membrane array. *A-A* shows typical fracture plane with small step at an E-face to P-face transition resulting from the assymetry of the location of the fracture plane in the membrane. *B-B*: some other fracture possibilities.

sheet. For example, in our terraced fractures it is commonly found that E-faces terminate, giving way to P-faces with very little shadow or illumination, implying a step in the fracture surface which is small compared to that observed for P-face to P-face or E-face to E-face jumps. This, along with the P- and E-face structures suggests the model shown in Fig. 17 for the fracture process in PM. We found no evidence for consistent orientational correlation of the hexagonal lattice of adjacent membrane sheets.

CONCLUSION

In this paper we have discussed the basic physical processes of and improved methodology for the production of multilayer arrays of biological membranes, systems which are finding wide use in biophysical membrane studies. We now conclude with several additional remarks. First, we have not discussed the question of membrane fusion which may occur in multilayer arrays of more fluid membranes, such as photoreceptor membrane discussed in two accompanying papers. Fusion may lead to arrays with enhanced orientational order. Secondly, we have not discussed polar membrane orientation which must be addressed if array useful for functional studies to be understood and produced. Experimentally, the methods described here could be adapted for polar orientation. For example, sedimentation in an electric field normal to the substrate surface will induce polar order in electrostatically asymmetric membrane fragments, such as purple membrane (39). Thirdly, the question of functional and structural integrity in lamellar arrays has not been addressed since this must be dealt with on a case by

case basis. For purple membrane kinetic absorption spectroscopy and resonant Raman studies of dried films indicate the presence of the same photo-intermediates as found in vitro, but with a somewhat altered kinetics. Similar results are found for photoreceptor membrane, as discussed in an accompanying paper (41, 42). Fourthly, the methods discussed here to probe array structure are not particularly sensitive to local 3-D ordering: intraplanar registration which may be induced in a well-ordered multilayer array. X-ray scattering studies of purple membrane arrays to date have indicated little 3-D ordering (8–9). However, in view of the apparent difficulty of forming three dimensional crystals from membrane proteins, it may be useful to view well oriented multilamellar arrays as a potential intermediate step in the formation of three dimensional membrane crystals. Detailed x-ray searches for the associated off-diagonal Bragg peaks would seem to offer the best hope for pursuing this possibility.

APPENDIX A

We consider what happens when thin disks (thickness = a, diameter = d, $a < 0.1\ d$) are pulled toward and cover at random a flat surface, e.g., suppose we throw pennies at random onto the floor of a large room. The first layer of disks lie flat on the surface and so have perfect orientational order. As disks are piled up they will rest unevenly on the ones nearer the surface so that $\delta\mathbf{n}$ for a typical disk will be nonzero.

The simplest approach to the calculation of $f(\theta, z)$ is to view the tilting of the disks as a random walk in which each disk, as it is added, can adopt an orientation differing from that of its neighbor below by an angle of magnitude a/d. The orientation at the top of a pile of depth D will be the result of $N \simeq D/d$ of these random steps of identical magnitude. The problem is equivalent to a two dimensional random walk in which the distribution of θ, the magnitude of the vector sum of N vectors, $\delta\mathbf{n}_i$, of magnitude a/d but of random direction, is to be obtained. The general result is (63):

$$f(\theta, z) = n[\pi N_z \langle \delta n_i^2 \rangle_z]^{-1} \exp\left\{\frac{-\theta^2}{N_z \langle \delta n_i^2 \rangle_z}\right\},$$

where, in the general case, $\langle \delta n_i^2 \rangle_z$ is calculated from the probability distribution of step sizes, $\mathcal{P}(\delta n_i, z)$. For this model $\mathcal{P}(\delta n_i, z) = \delta(\delta n_i - a/d)$ and

$$n_i = a/d, \tag{A1a}$$

$$N_z = z/a. \tag{A1b}$$

The mean square angular fluctuation is given in the general case by (39):

$$\langle \theta^2 \rangle_z = N_z \langle \delta n_i^2 \rangle_z, \tag{A2}$$

which for this model is

$$\langle \theta^2 \rangle_z = (z/a)\,(a/d)^2 = (za/d^2) \equiv (2z/3\xi_p). \tag{A3}$$

We have defined a penetration length, ξ_p:

$$\xi_p = 2d^2/3a, \tag{A4}$$

which will serve to indicate the penetration of the surface induced order into the array of disks. With this (somewhat arbitrary) choice the commonly defined orientational order parameter $\langle P_2(\theta) \rangle \equiv \langle \tfrac{1}{2}(3\cos^2\theta - 1) \rangle \simeq 1 - (3/2)\,\theta^2$ varies as $\langle P_2 \rangle_z = 1 - z/\xi_p$. Note that $\langle P_2 \rangle_s = \langle P_2 \rangle_{z=0} = 1$.

This "identical step" random walk calculation predicts orientational disorder sufficiently far from the

surface, a result of taking the contributions to $\delta\mathbf{n}$ to be a/d from all, even distant, disks. At sufficiently high disk densities, however, this assumption breaks down, as collective effects reduce the contributions of distant disks to the extent that $\langle\theta^2\rangle_z$ will remain finite at large z, i.e., there will be long range orientational order. To see this we need to know the orientational distribution function in a bulk sample of a "gas" of hard disks of number density n, a problem which has been treated (43, 64) using the methods developed by Onsager (65) to describe the orientational ordering of hard rods in solution. Calculations show that for thin disks ($a/d \ll 1$), when n is larger than a critical density $n^* \simeq 6d^{-3}$, there will be long range orientational order with a bulk order parameter $\langle P_2\rangle_B \gtrsim 0.8$ (63). Thus, once the volume available per disk gets to be small compared with d^3, the volume "excluded" by a single disk, orientational ordering will occur. This critical density is likely to be exceeded in any situation where anisotropic membrane fragments are being concentrated for orientation. An orientationally ordered array of disks, when bounded by a flat surface, will have minimum elastic energy when the average $\mathbf{n}$ is normal to the surface. In principle, therefore, a surface will generate long range order in an array with orientation fluctuations characterized by $\langle P_2\rangle_B$ away from the surface.

In the vicinity of the surface $\langle P_2\rangle$ will be larger, decreasing from $\langle P_2\rangle_s = 1$ at $z = 0$ to $\langle P_2\rangle_B$ at sufficiently large z. This spatial inhomogeniety can be treated using the Landau-deGennes theory of the nematic-isotropic phase transition (43) which yields the following variation of the orientational order parameter with distance from the surface, valid for both the ordered and isotropic ($\langle P_2\rangle_B = 0$) phases: $\langle P_2\rangle_z = \langle P_2\rangle_B + (\langle P_2\rangle_B)\exp(-z/\xi^*)$. For $z < \xi^*$ we recover the random walk dependence of Eq. 5: $\langle P_2\rangle_z \alpha z$. On the basis of the hard disk model we therefore expect a layer at the surface of thickness $\sim d^2/a$ which is "directly" ordered by the surface and if the concentration is high enough, long range order with a somewhat lower order parameter away from the surface. Whether the long range ordering is important will depend on the sample thickness D relative to d^2/a.

A serious deficiency of the hard disk model is that it ignores the flexibility and compressibility of the membranes. Allowing the disks to bend as they are pulled against the bottom surface leads to a more compact, layerlike array which has a reduced amount of orientational disorder.

APPENDIX B

We consider the membrane array to be a bulk smectic A liquid crystal having layer thickness a, layer compressional elastic constant B, and bulk layer curvature (splay) elastic constant K (43).

The cross section of an array of flexible, compressible membranes is shown schematically in Fig. 1 *b*. The effect of the finite fragment size is to introduce layer terminations that produce local tilt in the adjacent layers. Because of the membrane flexibility and compressibility this tilt decreases in magnitude but spreads over larger areas in the xy plane as the distance z from the layer termination increases (Fig. 2 *a*). The spatial variation of $\delta\mathbf{n}$ associated with a layer termination can be obtained by regarding the termination to be an edge dislocation in a smectic A liquid crystal. The layer distortion associated with a straight line edge dislocation can be calculated exactly and is shown schematically in Fig. 2 *a*. For a dislocation parallel to the y axis and located at $x = 0$, $z = 0$, as in Fig. 2 *a*, $\delta\mathbf{n}$ is given by (47, 48):

$$\delta n(x,z) = -a(4(\pi\lambda|z|)^{1/2})^{-1} \cdot \exp(-x^2/4\lambda|z|), \tag{B1}$$

where $\lambda = (K/B)^{1/2}$.

(B2)

In any plane parallel to the xz plane (the paper) substantial values of $\delta\mathbf{n}$ are confined to the inside of the parabola $x^2 < 4\lambda z$, the lightly shaded region in Fig. 2 *a*. In what follows below we shall replace the continuous δn of Eq. B1 by a more tractable approximate form in which for a given z, δn has a constant value within the parabola equal to its average and is zero outside (dashed layer, Fig. 2 *b*), i.e.,

$$\begin{aligned}\delta n(z) &= (a/2)(1/2w) = a/(8(\lambda|z|)^{1/2}), |x| < w = 2(\lambda|z|)^{1/2} \\ &= 0, |x| > w.\end{aligned} \tag{B3}$$

The characteristic length, λ, for typical values of K and B, is 20 nm $> \lambda >$ 2 nm and is expected to be comparable to the layer thickness, a (43). Since λ is so small (implying qualitatively that membranes are easy to bend but difficult to compress) the parabolic limit to the influence of the dislocation spreads only slowly: $w \simeq 0.6\ \mu$m for $\lambda = 10$ nm and $z = 10\ \mu$m.

A disk shaped fragment (diameter = d) in an array will act as a circular dislocation loop in a smectic A (Fig. 2 *c*). Close to the loop, for distances z such that $w(z) < d/2$ ($z < \xi \equiv d^2/16\lambda$) the distortion produced by the loop looks locally like that of a straight edge dislocation (48). However, in the far field, $w(z) \gg d/2$, all parts of the loop contribute to $\delta\mathbf{n}$, partially cancelling each other. In this limit if the loop is at the origin $\delta\mathbf{n}$ is largest near the paraboloid $x^2 + y^2 = 4\lambda|z|$, and falls off as $|z|^{-3/2}$, as compared with $|z^{-1/2}|$ for the straight edge dislocation from Eq. B3 (48).

To determine the orientational order in a membrane fragment array using this model we calculate the mean square fluctuation in layer orientation, $\langle \delta\theta^2 \rangle_{\Delta z}$ at a point $M = (x_0, y_0, z_0)$ induced by randomly placed dislocation loops in the region $|z_0 - z| < \Delta z$ in an infinite layer array. Because of the limited range of influence of a given edge dislocation only those dislocations which intersect the paraboloid of revolution given by $(x - x_0)^2 + (y - y_0)^2 = 4\lambda|z_0 - z|$ (Fig. 1 *b*) will contribute to $\delta\mathbf{n}$ at point M (M is not necessarily at the top of the array). We first consider the loops close enough to M so that $w < d/2$ will apply, i.e., the maximum paraboloid width will be small compared to the membrane fragment diameter, so that only a small portion of a given fragment edge will lie inside the paraboloid. We may then approximate the fragment edges by straight edge dislocations, and $\delta\mathbf{n}$ will be the sum of the statistically distributed contributions $\delta\mathbf{n}_i$ from each of these. The mean number of contributing dislocations having $|z - z_0| < \Delta z$, $N_{\Delta z}$, and the probability distribution of angular steps, $\mathcal{P}(\delta n_i, \Delta z)$ are given by:

$$N_{\Delta z} = 2\int_0^{\Delta z} dz(dN/dz) = 2\int_0^{\Delta z} dz(1/a)(2\pi w/d) = (8\pi/3)(w/d)(\Delta z/a), \tag{B4}$$

and

$$\begin{aligned} \mathcal{P}(\delta n_i, \Delta z) &= 3\delta n_c^3/\delta n_i^4 \qquad \text{for } \delta n_i > \delta n_c \\ &= 0 \qquad\qquad\quad \text{for } \delta n_i < \delta n_c. \end{aligned} \tag{B5}$$

Here δn_c is the magnitude of the smallest contributions to θ for $|z - z_0| < \Delta z$: $\delta n_c = a/(8(\lambda\,\Delta z)^{1/2})$. We can then obtain the mean square step size, $\langle \delta n_i^2 \rangle_{\Delta z}$, and, from Eq. A2, obtain $\langle \theta^2 \rangle_{\Delta z}$:

$$\left.\begin{aligned} \langle \delta n_i^2 \rangle_{\Delta z} &= (3/2)\delta n_c^2 = (3/128)(a^2/\lambda\Delta z) \qquad \text{(B6a)} \\ \langle \theta^2 \rangle_{\Delta z} &= (\pi/16)(aw/\lambda d) = (2\pi/16)(a/d)(\Delta z/\lambda)^{1/2} \qquad \text{(B6b)} \end{aligned}\right\} \Delta z < \xi.$$

Eq. B6b may be applied to surface orientation by introducing a surface (boundary condition $\delta\mathbf{n} = 0$) at $z = 0$. This boundary condition can be satisfied by the introduction of an appropriate image dislocation for each dislocation in the array (48) which also contributes to $\delta\mathbf{n}$ at each point in the array. The effect of the image dislocations is to effectively double the contributions of dislocations for $0 < z < z_0$ and cancel those for $z > 2z_0$. The effective $\langle \theta^2 \rangle$ is therefore increased by a factor of 2.5 and the result from Eq. B6b for $\langle \theta^2 \rangle$ a distance z above a flat surface becomes:

$$\langle \theta^2 \rangle_z \simeq (z/z^*)^{1/2} \quad z < \zeta = d^2/16\lambda \tag{B7}$$

with the characteristic length z^* defined as:

$$z^* \equiv d^2\lambda/a^2. \tag{B8}$$

As Δz increases beyond ξ such that $w > d/2$ the added contributions are primarily from whole loops which are intersected by the paraboloid centered on (x_0, y_0, z_0). For these, $N_{\Delta z}$ is unchanged from that of Eq. B4 but δn_c decreases more rapidly with z (i.e., as $|\Delta z|^{-3}$), rendering the net additional contribution to $\langle \theta^2 \rangle_{\Delta z}$ finite as $\Delta z \to \infty$. Thus the finite density of dislocation loops due to the finite fragment size does

not disrupt long range orientational order but induces a bulk variation of θ which may be obtained approximately from Eq. B6b by setting $w = d/2$:

$$\langle \theta^2 \rangle_B^{1/2} \sim \langle \theta^2 \rangle_{\Delta z}^{1/2} = (a/4\lambda)^{1/2}. \tag{B9}$$

We would like to thank D. Branton for the use of his freeze-fracture facilities, A. Fransoza, K. Rosen, V. Culbertson, and L. Duong for technical assistance, B. Becher, T. Ebrey, and K. Foster for purple membrane samples, and P. K. Brown for helpful discussions. This research was supported in part by grants from the Milton Fund of Harvard University and the National Science Foundation, Division of Materials Research, and from the National Institutes of Health, National Eye Institute.

Received for publication 17 December 1979 and in revised form 16 February 1980.

REFERENCES

1. BLASIE, J. K., M. M. DEWEY, A. E. BLAUROCK, and C. R. WORTHINGTON. 1965. Electron microscope and low angle x-ray diffraction studies on outer segment membranes from the retina of the frog. *J. Mol. Biol.* **14**:143–152.
2. LEVINE, Y. K., A. I. BAILEY, and M. H. F. WILKINS. 1968. Multilayers of phospholipid molecular leaflets. *Nature (Lond.).* **220**:577–578.
3. LEVINE, Y. K., and M. H. F. WILKINS. 1971. Structure of oriented lipid bilayers. *Nat. New Biol.* **230**:69–72.
4. LESSLAUER, W., J. E. CAIN, and J. K. BLASIE. 1972. X-ray diffraction studies of lecithin bimolecular leaflets with incorporated fluorescent probes. *Proc. Natl. Acad. Sci. U.S.A.* **69**:1499–1503.
5. BLAUROCK, A. E., and W. STOECKENIUS. 1971. Structure of the purple membrane. *Nat. New Biol.* **233**:152–155.
6. BLASIE, J. K. 1972. The location of photopigment molecules in the cross section of frog retinal receptor disk membranes. *Biophys. J.* **12**:191–204.
7. STAMATOFF, J. B., S. KRIMM, and N. R. HARVIE. 1975. X-ray diffraction studies of human erythrocyte structure. *Proc. Natl. Acad. Sci. U.S.A.* **72**:531–534.
8. HENDERSON, R. 1975. The structure of purple membrane from *Halobacterium Halobium:* analysis of the X-ray diffraction pattern. *J. Mol. Biol.* **93**:123–137.
9. BLAUROCK, A. E. 1975. Bacteriorhodopsin: a trans-membrane pump containing alpha-helix. *J. Mol. Biol.* **93**:139–158.
10. WORCHESTER, D. L., and N. P. FRANKS. 1976. Structural analysis of hydrated egg lecithin and cholesterol bilayers: I. X-ray diffraction and II. Neutron diffraction. *J. Mol. Biol.* **100**:345–378.
11. HERBETTE, L., J. MARQUARDT, A. SCARPA, and J. K. BLASIE. 1977. A direct analysis of lamellar x-ray diffraction from hydrated multilayers of fully functional sarcoplasmic reticulum. *Biophys. J.* **20**:245–252.
12. KHARE, R. S., and C. R. WORTHINGTON. 1977. An X-ray diffraction study of sphingomyelin-cholesterol interaction in oriented bilayers. *Mol. Cryst. Liq. Cryst.* **38**:195–206.
13. ZACCAI, G., J. K. BLASIE, and B. P. SCHOENBORN. 1975. Neutron diffraction studies on the location of water in lecithin bilayer model membranes. *Proc. Natl. Acad. Sci. U.S.A.* **72**:376–380.
14. SCHOENBORN, B. P. 1976. Neutron scattering for the analysis of membranes. *Biochim. Biophys. Acta.* **457**:41–55.
15. NEUGEBAUER, D. C., A. E. BLAUROCK, and B. L. WORCHESTER. 1977. Magnetic orientation of purple membranes demonstrated by optical measurements and neutron scattering. *FEBS Lett.* **78**:31–35.
16. HERBETTE, L., A. SCARPA, B. SCHOENBORN, and J. K. BLASIE. 1978. Analysis of the lamellar neutron diffraction from functional sarcoplasmic reticulum. *Biophys. J.* **21**:205 *a.* (Abstr.).
17. SAXENA, A. M., and B. P. SCHOENBORN. 1977. Neutron diffraction studies of the structure of oriented dipalmitoyl lecithin multilayers. *Biophys. J.* **17**:47 *a.* (Abstr.).
18. POWERS, L., and N. A. CLARK. 1975. Preparation of large monodomain phospholipid bilayer smectic liquid crystals. *Proc. Natl. Acad. Sci.* **72**:840–848.
19. LEPESANT, J. P., L. POWERS, and P. S. PERSHAN. 1978. Brillouin light scattering measurements of the elastic properties of aligned multilamellar lipid samples. *Proc. Natl. Acad. Sci.* **75**:1792–1795.
20. CHAN, W. K., and P. S. PERSHAN. 1978. Lipid and thermal diffusivity in a lipid-water smectic phase. *Biophys. J.* **23**:427–449.

21. LIBERTINI, L. J., A. S. WAGGONER, P. C. JOST, and O. H. GRIFFITH. 1969. Orientation of lipid spin labels in lecithin multilayers. *Proc. Natl. Acad. Sci.* **64**:13–19.
22. HUBBELL, W. L., and H. M. MCCONNELL. 1969. Orientation and motion of amphiphilic spin labels in membranes. *Proc. Natl. Acad. Sci.* **64**:20–27.
23. SEELIG, J. 1970. Spin label studies of oriented smectic liquid crystals (a model system for bilayer membranes). *J. Am. Chem. Soc.* **92**:3881–3887.
24. CHARVOLIN, J., P. MANNEVILLE, and B. DELOCHE. 1973. Magnetic resonance of perdeuterated potassium laurate in oriented soap-water multilayers. *Chem. Phys. Lett.* **23**:345–348.
25. GRIFFIN, R. G., L. POWERS, and P. S. PERSHAN. 1978. Head-group conformation in phospholipids: a phosphorous 31 nuclear magnetic resonance study of oriented monodomain dipalmitoylphosphatidylcholine bilayers. *Biochemistry.* **17**:2718–22.
26. SEELIG, J. 1978. ^{31}P nuclear magnetic resonance and the head group structure of phospholipids in membranes. *Biochim. Biophys. Acta.* **515**:105–140.
27. CHERRY, R. J., K. HSU, and D. CHAPMAN. 1972. Polarized absorption spectroscopy of chlorophyll-lipid membranes. *Biochim. Biophys. Acta.* **267**:512–522.
28. YGUERABIDE, J., and L. STRYER. 1971. Fluorescence spectroscopy of an oriented model membrane. *Proc. Natl. Acad. Sci.* **68**:1217–1221.
29. GEANCINTOV, N. E., F. VAN NOSTRAND, M. POPE, and J. B. TINKEL. 1971. Magnetic field effect on the chlorophyll fluorescence in chorella. *Biochim. Biophys. Acta.* **226**:486–491.
30. WRIGHT, W. E., P. K. BROWN, and G. WALD. 1972. The orientation of rhodopsin and other pigments in dry films. *J. Gen. Physiol.* **59**:201–212.
31. HEYN, M. P., R. J. CHERRY, and U. MULLER. 1977. Transient and linear dichroism studies on bacteriorhodopsin: determination of the orientation of the 568 nm all-*trans* retinal chromophore. *J. Mol. Biol.* **117**:607–620.
32. MUCCIO, D. D., and J. Y. CASSIM. 1979. Interpretation of the absorption and circular dichroic spectra of Oriental purple membrane films. *Biophys. J.* **26**:427–440.
33. ROTHSCHILD, K. J., and N. A. CLARK. 1979. Polarized infrared spectroscopy of oriented purple membrane. *Biophys. J.* **25**:473–488.
34. POWERS, L., and P. S. PERSHAN. 1977. Monodomain samples of dipalmitoyl phosphatidycholine with varying concentrations of water and other ingredients. *Biophys. J.* **20**:137–1.
35. BANGHAM, A. D., and R. W. HORNE. 1964. Negative staining of phospholipids and their structural modification by surface-active agents as observed in the electron microscope. *J. Mol. Biol.* **8**:660–668.
36. BOGOMOLNI, R., S. B. HWANG, Y. W. TSENG, and W. STOECKENIUS. 1978. Linear and circular dichroism of oriented purple membranes. *Biophys. J.* **21**:183.
37. KORENBRAT, J. I., and M. PRAMIK. 1977. Formation, structure, and spectrophotometry of air-water interface films containing rhodopsin. *J. Membr. Biol.* **37**:235–62.
38. HWANG, S. B., U. I. KORENBRAT, and W. STOECKENIUS. 1977. Structural and spectroscopic characteristics of bacteriorhodopsin in air-water interface films. *J. Mem. Biol.* **36**:115–35.
39. NAGY, K. 1978. Photoelectric activity of dried, oriented layers of purple membrane from *Halobacterium Halobium. Biochem. Biophys. Res. Commun.* **85**:383–395.
40. KUHN, H., D. MOBIUS, and H. BUCHER. 1972. Spectroscopy of monolayer assemblies, in *Physical Methods of Chemistry*, ed. A. Weissberger and B. W. Rossiter (Wiley, N.Y.) vol. I, part 3B.
41. ROTHSCHILD, K. J., N. A. CLARK, and K. ROSEN. 1980. Incorporation of photoreceptor membrane into a multilamellar array. *Biophys. J.* **31**:45–52.
42. ROTHSCHILD, K. J., R. SANCHES, T. L. HSIAO, and N. A. CLARK. 1980. Orientation of rhodopsin alpha-helices. *Biophys. J.* **31**:53–64.
43. DEGENNES, P. G. 1974. The Physics of Liquid Crystals. (Oxford University Press, London). Ch. 7.
44. DEGENNES, P. G. 1969. Conjectures on the smectic state. *J. Physiol. (Paris).* **30-C4**:65–72.
45. CLARK, N. A. 1976. Pretransitional mechanical effects in a smectic A liquid crystal. *Phys. Rev. A* **14**:1551–4.
46. HELFRICH, W. 1973. Elastic properties of lipid bilayers: theory and possible experiments. *Z. Naturforsch.* **28c**:693–703.
47. DEGENNES, P. G. 1972. Edge Dislocations in Smectics A. *C. R. Acad. Sci. Paris.* **B275**:939–941.
48. PERSHAN, P. S. 1974. Dislocation effects in smectic-A liquid crystals. *J. Appl. Physiol.* **45**:1590–1604.
49. DEULING, H. J., and W. HELFRICH. 1976. Red blood cell shapes as explained on the basis of curvature elasticity. *Biophys. J.* **16**:861–868.
50. DEULING, H. J., and W. HELFRICH. 1976. The curvature elasticity of fluid membranes: a catalogue of vesicle shapes. *J. Physiol. (Paris).* **37**:1335–1345.
51. HARBICH, W., H. J. DEULING, and W. HELFRICH. 1977. Optical observation of rotationally symmetric lecithin vesicle shapes. *J. Physiol. (Paris).* **38**:727–730.

52. GEBHART, C., H. GRULER, and E. SACKMANN. 1977. On domain structure and local curvature in lipid bilayers and biological membranes. *Z. Naturforsch.* **32**:581–596.
53. HELFRICH, W. 1978. Self interaction of fluid membranes in multilayer systems. *Z. Naturforsch.* **33a**:305–315.
54. JAIN, M. K. 1972. The bimolecular lipid membrane. Van Nostrand Reinhold, N.Y.
55. DEVRIES, A. J. 1958. Foam stability. IV. Kinetics and activation energy of film rupture. *Rec. Trav. Chim.* **77**:383–399.
56. DEVRIES, A. J. 1958. Foam stability. V. Mechanism of film rupture. *Rec. Trav. Chim.* **77**:441–461.
57. TAUPIN, C., M. DVOLAITZKY, and C. SAUTEREY. 1975. Osmotic pressure induced pores in phospholipid vesicles. *Biochemistry.* **14**:4771–4.
58. ELWORTHY, P. H. 1961. The adsorption of water vapor by lecithin and lysolecithin, and the hydration of lysolecithin micelles. *J. Chem. Soc. (Lond.)* **1961**:5385.
59. BECHER, B., and J. Y. CASSIM. 1975. Improved isolation procedures for the purple membrane of *Halobacterium Halobium. Prep. Biochem.* **5**:161–1.
60. HENDERSON, R., and P. N. T. UNWIN. 1975. Three-dimensional model of purple membrane obtained by electron microscopy. *Nature (Lond.).* **257**:28–32.
61. FISHER, K. A., and W. STOECKENIUS. 1977. Freeze-fractured purple membrane particles: protein content. *Science (Wash. D. C.).* **197**:72–74.
62. FISHER, K. A., K. YANAGIMOTO, and W. STOECKENIUS. 1978. Oriented adsorption of purple membrane to cationic surfaces. *J. Cell Biol.* **77**:611–621.
63. CHANDRASEKHAR, S. 1943. Stochastic problems in physics and astronomy. *Rev. Mod. Phys.* **15**:2–89.
64. ONSAGER, L. 1949. The effects of shape on the interaction of colloidal particles. *Ann. N.Y. Acad. Sci.* **51**:627–659.
65. FORSYTH JR., P. A., S. MARCELJA, D. J. MITCHELL, and B. W. NINHAM. 1978. Ordering in colloidal systems. *Adv. Coll. Int. Sci.* **9**:37–60.